

Czech Technical University
Faculty of Electrical Engineering
Department of Control Engineering



Sensor Fusion Solutions for Upcoming CubeSat Missions

Mariana Barbosa

Prague, June 2013

Supervisor: **Prof. Dr. Martin Hromcik**

Examiner: **Prof. Dr. Anita Enmark**

Supervisor USU: **Prof. Dr. Rees Fullmer**

Czech Technical University in Prague
Faculty of Electrical Engineering

Department of Control Engineering

DIPLOMA THESIS ASSIGNMENT

Student: **De Magalhaes Rodrigues Barborsa Mariana**

Study programme: Cybernetics and Robotics
Specialisation: Systems and Control

Title of Diploma Thesis: **Sensor fusion solutions for upcoming cubesat missions.**

Guidelines:

The thesis is devoted to advanced algorithms for sensor fusion applied to the case of a small satellite. Severe limitations regarding sensors accuracy due to limited size and budget constraints shall be taken into account. The thesis is conducted at the Space Dynamics Lab of the Utah State University, USA, under technical supervision of Prof. Rees Fullmer.

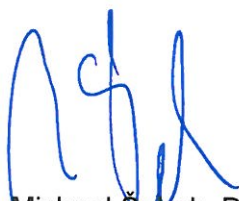
1. Get familiar with the Kalman filter in the linear and nonlinear case and its application for data fusion problems.
2. Develop and implement algorithms based on Kalman filter for estimation of a small satellite attitude.
3. Validate selected algorithms by simulation and/or experiments.

Bibliography/Sources:

Literature: B.D.O. Anderson, Optimal Filtering, Springer Verlag, Berlin, 1990.

Diploma Thesis Supervisor: Ing. Martin Hromčík, Ph.D.

Valid until the summer semester 2013/2014


prof. Ing. Michael Šebek, DrSc.
Head of Department




prof. Ing. Pavel Ripka, CSc.
Dean

Prague, January 15, 2013

Abstract

In this thesis, an extended Kalman filter formulation for attitude estimation is developed for implementation in a small satellite simulator using inertial sensors. Two different attitude parametrizations are analyzed: quaternions and modified Rodrigues parameters. Simulations and experiments are conducted to validate each Kalman filter algorithm. This thesis also investigates the deterministic and random error sources of sensors measurements. A calibration procedure is proposed and conducted to eliminate the deterministic error sources. The random error is modeled with the Allan variance formulation and it is integrated in the Kalman filter. The results for the simulations with both attitude parametrizations are found to yield accurate attitude solutions. The advantage of the quaternion approach is that it does not have singularities, while the advantage of the modified Rodrigues parameters approach is that it is simpler since it has one less state. Experimental tests were conducted on a one-degree of freedom air bearing. The results from experimentation indicate that in reality, the filter results in a less accurate attitude solution than predicted by simulation. Suggestions to improve the filter performance are proposed.

Proclamation:

I hereby attest that all content present in this thesis is a result of my own work whereas all used previous material and references are duly indicated.

In Prague, May 31, 2013

.....

Mariana Barbosa

Acknowledgments

Firstly, I would like to thank my supervisor in Utah State University Dr. Rees Fullmer, who gave me the opportunity to work on this interesting project, for his guidance over the short time this thesis was conducted. Also, many thanks to my supervisor in Czech Technical University, Dr. Martin Hromcik, who first introduced me to the stochastic models and Kalman filtering.

Very helpful mechanical support was given by Landon Terry. I am grateful for the manufacturing of a level platform and of a structure for the IMUs.

I wish to express my sincere appreciation to Jan Sommer, the electrical engineer, for the design of the electronics. I owe a lot of credit specially for the development of the BB data acquisition software and for helping me with Latex.

Last but not least, I would like to thank Marina Samuels for her suggestions during the process of writing.

Contents

1	Introduction	1
1.1	Main Objective	3
1.2	Overview	3
1.3	Structure of the Thesis	4
2	Theoretical Background	5
2.1	Coordinate Frames	5
2.2	Attitude Representation	7
2.2.1	Quaternions	7
2.2.1.1	Quaternions Representing Rotations	8
2.2.2	Modified Rodrigues Parameters	9
2.3	The Kalman Filter	10
2.3.1	The Discrete Kalman Filter	10
2.3.2	The Discrete Extended Kalman Filter	12
3	Calibration	16
3.1	Calibration Concept	18
3.2	Sensor Error Model	18
3.2.1	Scale factor	18
3.2.2	Bias	18
3.2.3	Non-orthogonality	19
3.2.4	Sensor Error Model Equation	19
3.3	Calibration Algorithm	20
3.4	The Magnetometer Case	21
3.4.1	Magnetometer Calibration Algorithm	22

3.5	Procedures and Results	23
3.5.1	Accelerometer	24
3.5.2	Gyroscope	27
3.5.3	Magnetometer	28
4	Sensor Noise Model	31
4.1	Sensor Noise Model Equation	31
4.2	Allan Variance Definition	32
4.3	Allan Deviation Plots	33
4.4	Noise in terms of Allan Variance	35
4.4.1	White Noise Part	35
4.4.2	Exponentially Correlated Noise Part	36
4.5	Example	37
4.5.1	White noise part	38
4.5.2	Exponentially Correlated Noise Part	38
4.5.3	Final Model	40
4.6	Results	40
5	Kalman Filter Design	43
5.1	Introduction	43
5.2	Attitude Kinematics	44
5.2.1	Rigid Body Dynamics	44
5.2.2	Rigid Body Orientation	45
5.3	Pre-filter step	45
5.4	Sensor Model	46
5.5	First Approach	47
5.5.1	The State Vector	47
5.5.2	State Equations	48
5.5.3	The Outputs	49
5.6	Second Approach	50
5.6.1	The State Vector	50
5.6.2	State Equations	51
5.6.3	The Outputs	51

5.7	Extended Kalman Filter Loop	51
5.7.1	Initialization	51
5.7.2	The Loop	53
6	Implementation and Testing	54
6.1	Simulation Environment	54
6.1.1	Generation of the Simulated Measurements	54
6.1.2	Kalman Filter Estimation	56
6.1.2.1	Quaternion Approach	56
6.1.2.2	Modified Rodrigues Parameters Approach	58
6.1.3	Conclusions about the Simulations	61
6.2	Test with the Air-Bearing Table	62
7	Conclusions and Future Work	68
7.1	Summary	68
7.2	Analysis of Results	68
7.3	Future Work	69
A	Kalman Filter Matrices	74
A.1	First Approach	74
A.2	Second Approach	75

List of Figures

1.1	Preliminary design of the satellite simulator.	1
1.2	Diagram of electronics and communication.	2
1.3	Kalman filter scheme.	3
2.1	Earth inertial and body frame coordinate axes.	6
2.2	Sensors coordinate system.	7
2.3	Rotation using quaternions.	9
2.4	Diagram with the operations of the discrete Kalman filter. Adapted from [26].	13
2.5	Diagram with the operations of the extended Kalman filter. Adapted from [26].	15
3.1	Pictures of the IMUs used in the project.	16
3.2	IMUs mounted in a aluminum structure.	17
3.3	Sensor sensitivity axes and body frame coordinate axes.	19
3.4	Ellipsoid data leads to calibrated measurements lying on the sphere. From [24].	23
3.5	Diagram with the IMUs, the encoder, and its interfaces with the computer	24
3.6	Leveled platform used to calibrate the accelerometers.	25
3.7	6 positions of the accelerometer calibration. From [11].	25
3.8	Accelerometer calibration of the Pololu IMU.	26
3.9	Accelerometer calibration of the MicroStrain IMU.	26
3.10	Air bearing table.	28
3.11	Gyroscope calibration of the Pololu IMU.	29
3.12	Gyroscope calibration of the MicroStrain IMU.	29
3.13	Magnetometer calibration results, in Gauss.	30
4.1	Example of the data structure used to derive Allan variance.	33

4.2	Allan deviation for the acceleration data for both IMUs.	34
4.3	Allan deviation for the angular rate data for both IMUs.	34
4.4	Allan deviation for the magnetic field data for both IMUs.	35
4.5	$\sigma(\tau)$ plot for bias instability. From [30].	37
4.6	y-axis gyro output from MicroStrain 3DM-GX3-25.	38
4.7	White noise part of the Allan deviation in comparison with the total.	39
4.8	Auto-correlation function of the Allan deviation of the exp. correlated noise.	39
4.9	Real signal compared with the simulated signal.	41
5.1	Block diagram of the first approach of the Kalman filter.	47
5.2	Block diagram of the second approach of the Kalman filter.	50
5.3	EKF loop. Based on [2].	53
6.1	Simulated measurements.	55
6.2	Quaternions of the simulation.	56
6.3	Euler angles of the first approach simulation.	57
6.4	Covariances of the first approach simulation.	57
6.5	Angle of rotation errors of the quaternion simulation.	58
6.6	Modified Rodrigues Parameters.	59
6.7	Euler angles of the second approach simulation.	60
6.8	Covariances of the second approach simulation.	60
6.9	Angle of rotation errors of the MRP simulation.	61
6.10	Level planar air bearing with mounted sensors and BB.	62
6.11	Measurements from IMUs and encoder.	63
6.12	True and estimated quaternions.	64
6.13	True and estimated Euler angles.	64
6.14	Covariances of the quaternions.	65
6.15	Covariances of the bias of the MicroStrain instrument.	65
6.16	Covariances of the bias of the Pololu instrument.	66
6.17	Angle of rotation errors of the test.	67

List of Tables

4.1	Noise coefficients for MicroStrain sensor	41
4.2	Noise coefficients for MicroStrain sensor	42

Nomenclature

ADCS Attitude Determination and Control System

BB Beagle Bone

EKF Extended Kalman Filter

IMU Inertial Measurement Unit

MEMS Micro-Electro-Mechanical System

MRP Modified Rodrigues Parameters

SDL Space Dynamics Laboratory

Chapter 1

Introduction

A small satellite simulator with precise three-axis attitude determination and control is being designed and implemented in hardware. The simulator consists of inertial sensors and a star camera for attitude determination, and a pyramidal four-wheel momentum exchange system as the control actuators. The preliminary desing of the table can be seen in Figure 1.1. The simulator is predicted to be placed on a spherical air bearing platform to allow three-degree-of-freedom operation.

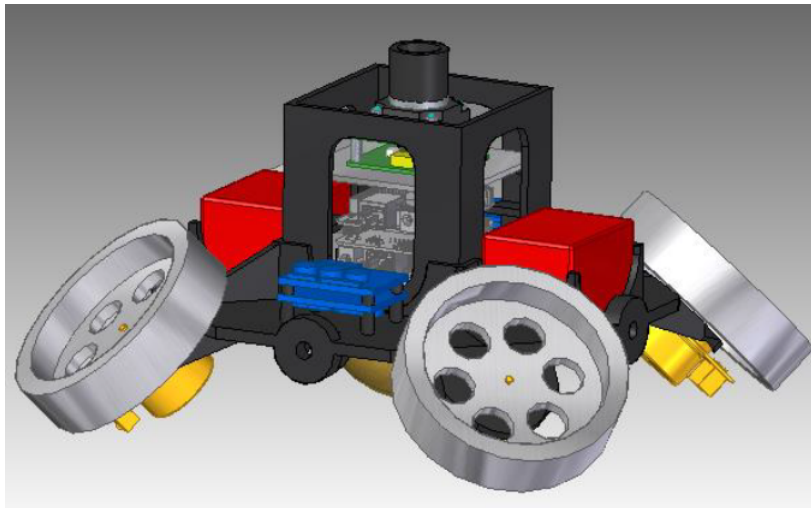


Figure 1.1: Preliminary design of the satellite simulator.

The electronic design is divided into two separate units with each having its own computational platform: one for the star camera and the other for the attitude determination and control system (ADCS). Each platform has a separate Beagle Bone (BB) microcomputer, driven by a 720 MHz ARM-CPU. A schematic block diagram of the connections is presented in Figure 1.2. One BB will be connected to the motor controllers and sensors, while the other will be connected to the star camera via USB inter-

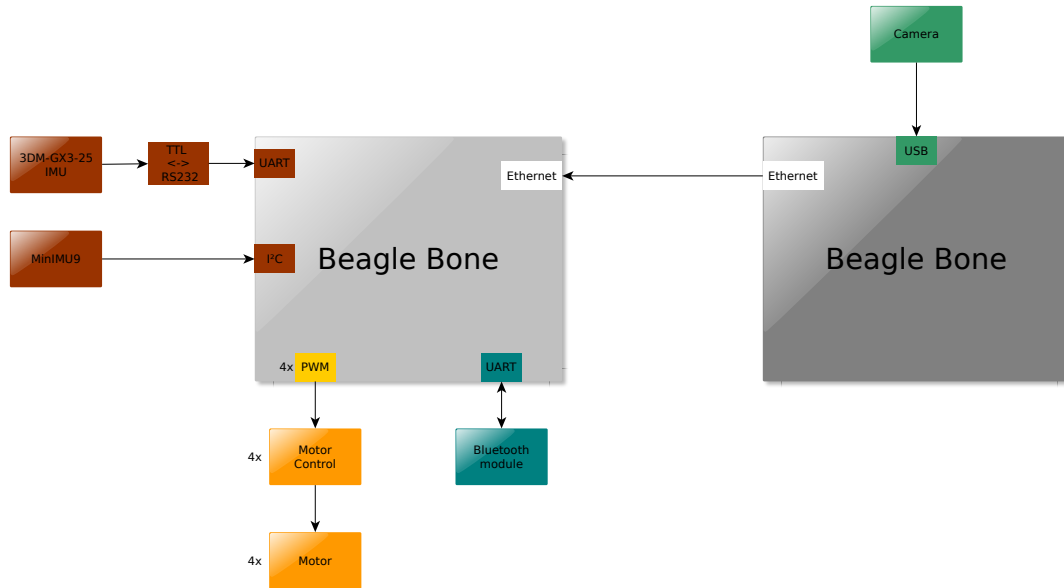


Figure 1.2: Diagram of electronics and communication.

face. An Ethernet cable provides communication between the two boards.

The board of the attitude determination control system is responsible for the general state estimate by running the sensor inputs through the Kalman filter. Two inertial measurement units (IMUs) will be used for comparison purposes. The first is the low level, low cost MinIMU9v2, connected to the board via the I²C interface. The second IMU is the 3DM-GX-25-IMU from Microstrain. This latter IMU uses a RS232-serial connection. After the state estimate is obtained, the appropriate control commands are then calculated through the controller algorithm. These control commands are then outputted as PWM signals to the motor controllers, which regulate motor current and speed. In addition, analog feedback signals from the motors will be connected to the board to be incorporated in the control algorithm. A simple Bluetooth modem is connected to a second serial port of the BB, so that the reference of the control (desired orientation/position) can be sent wirelessly.

This project is supported by the Space Dynamics Laboratory (SDL) from the Utah State University. The SDL has launched its own Cubesats into space with the main objective to measure magnetic disturbances in Earth's ionosphere. In order to improve its Cubesats capabilities for future missions, the SDL is supporting the development of small satellites technologies, with major focus on precision attitude determination and control. As such, the design and implementation of this small satellite simulator is a valuable and relevant research tool.

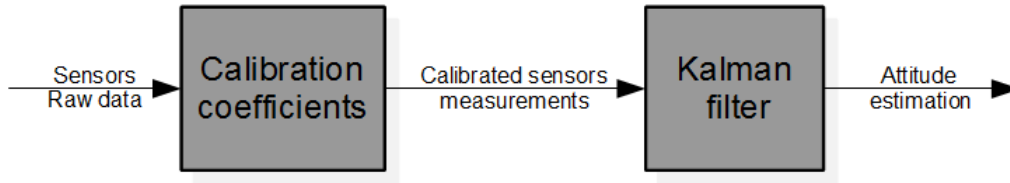


Figure 1.3: Kalman filter scheme. The raw measurement is corrected by static calibration coefficients and the result is used as the input of the Kalman filter, given the estimated attitude as output.

1.1 Main Objective

The main objective of this thesis consists in the development of a Kalman filter using inertial sensors inputs provided by two different IMUs. The thesis results will be a working attitude determination system.

1.2 Overview

The task of attitude estimation of the spacecraft involves:

- 1) estimation of its orientation relative to some reference frame and
- 2) combining measurements and models.

The first part is accomplished by obtaining a set of parameters that relates the angular position from body frame with respect to a non-moving (or inertial) frame, i.e., obtaining an attitude representation of the spacecraft. This representation is performed in this thesis using quaternions and modified Rodrigues parameters.

The second part is achieved by combining the measurements with dynamic models, which can be done in several different ways. A common way is to fuse data from rate gyros and other attitude sensors [3, 16], e.g., magnetometers and accelerometers. The inertial measurement units can be used to measure the spacecraft angular velocity, the magnetic field and the acceleration with respect to an inertial frame. Hence, modeling and calibration of the sensors become a significant part of the attitude determination problem. In this project, the extended Kalman filter will be used to combine or “fuse” sensor measurements with dynamic models in order to obtain the optimal attitude estimation. Figure 1.3 illustrates in a block diagram the overview scheme with the steps to achieve the attitude estimation.

The objectives of the thesis could be further broken into:

1. Characterize sensor measurements in terms of deterministic and random errors for both IMUs. The inertial sensor errors can be divided into two parts: deterministic and random. The deterministic error sources include the bias, the scale factors, and the misalignment errors. The ran-

dom errors include white noise and exponentially correlated noise.

2. Develop a Kalman filter in a simulation environment, using both quaternions and modified Rodrigues parameters. Models of the sensors are also going to be implemented based on the noise characteristics. The performance of the filters is going to be compared.
3. Experimental testing of the performance of the filter using a one-axis rate table.

1.3 Structure of the Thesis

The thesis is organized as follows:

- Chapter 2 reviews the concepts of frames and introduces the notion of quaternions and modified Rodrigues parameters, showing how they both can represent rotations. It also reviews the basics of Kalman Filters.
- Chapter 3 explains the calibration procedure used to find the deterministic error sources of the sensors and presents the results.
- Chapter 4 develops the sensor noise model and presents the results. The Allan Variance method will be applied in determining those sources of errors.
- Chapter 5 is the core of this thesis. The Kalman filter formulations using both quaternions and modified Rodrigues parameters are derived.
- Chapter 6 describes the filter simulation and tests with real measurements. It explains how simulated data were created and discusses the results of applying that data to the filters. It also presents the experimental setup, the measurement procedure and the results.
- Chapter 7 presents a short summary along with an analysis of results and conclusions. It ends with suggestions for the future work.

Chapter 2

Theoretical Background

The attitude estimation of the spacecraft involves a two-part process: estimation of its orientation from body measurements relative to some reference frame and filtering of measurements. The first part is accomplished by obtaining an attitude representation of the spacecraft. A very complete review of attitude representations can be found in the survey paper by Shuster [21]. The second part is achieved by combining the measurements with models, which can be done in several different ways as shown Crassidis and others in the survey paper [6]. In this thesis, the filtering which will be used is the extended Kalman filter.

This chapter presents the concepts of coordinate frames (section 2.1) and gives an overview on well-known attitude representation methods (section 2.2). Section 2.3 presents the basics of Kalman filtering and discusses the formulation and structure of the extended Kalman filter.

2.1 Coordinate Frames

Many Cartesian coordinate systems are used in spacecraft related applications, as explained in [27]. This section presents the two frames used in this thesis:

- The Earth inertial frame, fixed with its origin at the center of the Earth, with z-axis pointing to geographic North, x-axis points in the direction of vernal equinox and the y-axis completes the right-handed orthogonal system [27].
- The body frame, which is a coordinate frame attached to the body (in this case the simulation satellite). The origin of the body-fixed frame is the center of mass of the satellite. The fixed x-axis (or roll), y-axis (or pitch), and z-axis (or yaw) define the orientation of the attitude. Let u be the

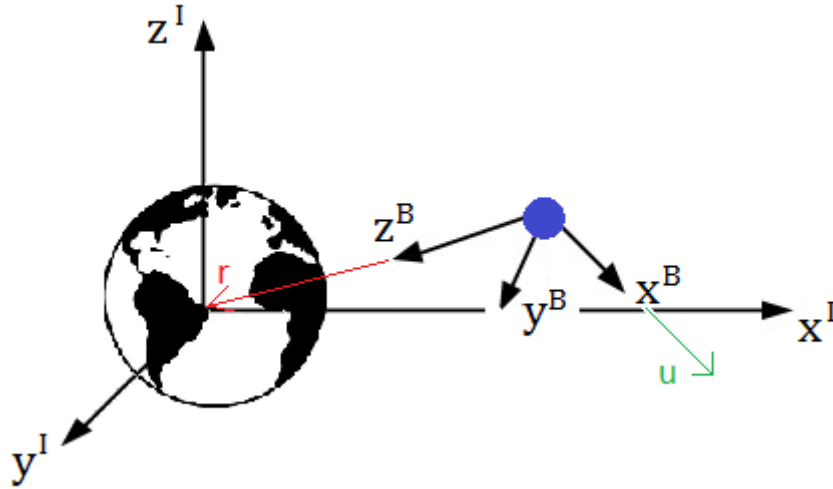


Figure 2.1: Earth inertial frame coordinate axes $[x^I \ y^I \ z^I]^T$ and body frame coordinate axes $[x^B \ y^B \ z^B]^T$.

vector of spacecraft velocity, r be the vector from the spacecraft to the Earth center. By convention, the x-axis is selected along with the velocity direction, the z-axis is in the direction of r , and the y-axis follows the right-hand rule [27].

There are two different forms to mount the sensors in an inertial system, and the main distinction is whether or not the sensors are fixed to the spacecraft and its corresponding body coordinate system. In the first type, the inertial sensors are mounted on a stable platform, which is connected to gimbals. The platform is maintained leveled and headed in a fixed direction. Alternatively, the inertial sensors can be fixed to the spacecraft, known as "strapdown" mechanization. The strapdown option is used in this work, and each measurement with respect to body frame must be converted into inertial axes. Therefore, the coordinate transformation between frames is very important and will be analyzed in the next section.

It is important to note that the satellite simulator was not assembled during the time that this thesis was written. As a result, the body frame adopted in this thesis is the frame defined by the sensors vendor. Figure 2.2 illustrates the sensor coordinate frames from each IMU. After the assembly of the satellite, the sensors must be mounted in alignment with the satellite's body coordinate system. However, small misalignment due to mounting may occur and they must be corrected via a calibration procedure with the goal to make the sensors measurements perfectly aligned with the satellite's body frame.

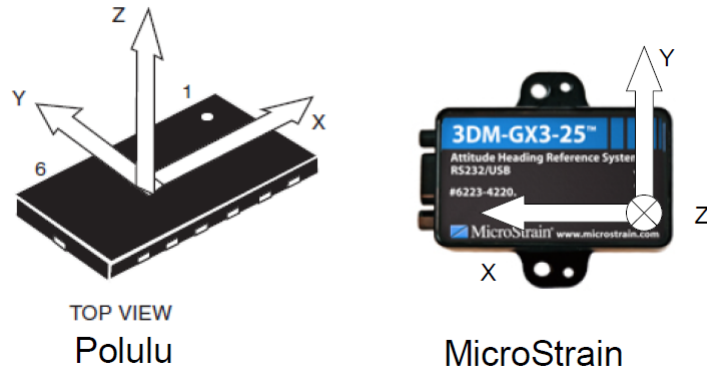


Figure 2.2: Sensors coordinate system.

2.2 Attitude Representation

Any vector can be represented in a coordinate frame by three components. These components are the projections of the vector along each of the frame axes. Given the components of a vector in one frame, the components in another frame can be calculated provided that the relationship between the frames is known.

Let v^B and v^I be vectors in body and inertial frames respectively. The rotation matrix R_I^B , often referred to as the direction cosine matrix or attitude matrix, is given by [21]:

$$v^B = R_I^B v^I. \quad (2.1)$$

The rotation matrix is an 3×3 orthogonal and proper matrix. Rotation matrices contain redundant information, and the same information provided by the 9 element matrix can be obtained from other many attitude parametrizations. Examples are the Euler angles, the Rodrigues parameters (Gibb's vector), the quaternions, and the modified Rodrigues parameters, among others, as discussed in the attitude representation survey by Shuster [21].

Both modified Rodrigues parameters and quaternions are employed here, and they will be discussed in detail in next subsections.

2.2.1 Quaternions

In 1843, Hamilton invented a 4 dimensional vector, to which he gave the name quaternion. It is defined as

$$q \equiv \begin{bmatrix} q_0 & q_1 & q_2 & q_3 \end{bmatrix}^T = \begin{bmatrix} q_0 \\ \vec{q} \end{bmatrix}, \quad (2.2)$$

or can be represented by a hyper-complex number

$$q \equiv q_0 + q_1 i + q_2 j + q_3 k, \quad (2.3)$$

where q_0, q_1, q_2, q_3 are real numbers and i, j, k are imaginary numbers with the property $i^2 = j^2 = k^2 = ijk = -1$. Also, i, j, k can be interpreted as unit vectors directed along the $x, y,$ and z axis respectively. Therefore, the quaternion is the sum of a scalar and a 3-dimensional vector.

Using the hyper-complex definition, it can be shown that the product between two quaternions q and r is [21]

$$q \otimes r = \pm \begin{bmatrix} q_0 r_0 - \vec{q} \cdot \vec{r} \\ q_0 \vec{r} + r_0 \vec{q} - \vec{q} \times \vec{r} \end{bmatrix}. \quad (2.4)$$

This operation is known as a quaternion multiplication. Traditionally, one chooses the positive sign in equation (2.4) [21].

2.2.1.1 Quaternions Representing Rotations

A quaternion $q_0 + q_1 i + q_2 j + q_3 k$ such that

$$q_0 = \cos\left(\frac{\theta_r}{2}\right), \quad \vec{q} = \hat{n} \cdot \sin\left(\frac{\theta_r}{2}\right), \quad (2.5)$$

can be used to rotate an arbitrary vector v . The unit vector \hat{n} is the axis of rotation and θ_r is the angle of rotation [16, 21]. From equation (2.5), it is clear that the quaternion q must have a unit norm and, consequently, it has only three degrees of freedom.

In order to perform the rotation, first the vector v must be written as a pure quaternion:

$$v = v_0 + \vec{v} = 0 + \vec{v}. \quad (2.6)$$

The rotation is performed through the double quaternion multiplication

$$v^R = q \otimes v \otimes q^*, \quad (2.7)$$

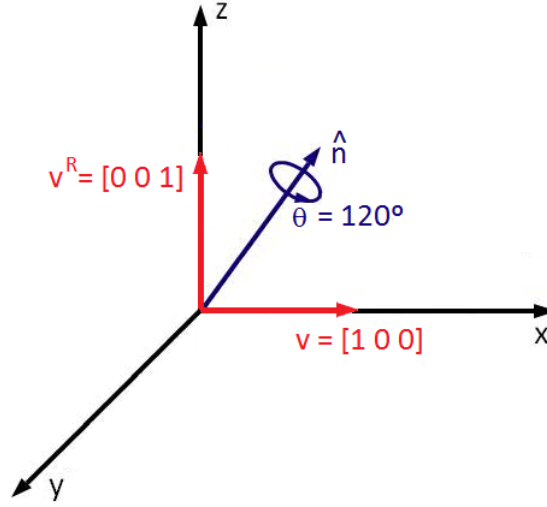


Figure 2.3: Rotation using quaternions.

where v^R is the vector v rotated and q^* is the complex conjugate of the quaternion q , defined as

$$q^* = q_0 - q_1 i - q_2 j - q_3 k. \quad (2.8)$$

The operation in equation (2.7) is equivalent with the direction cosine matrix multiplication

$$v^R = R(q)v, \quad (2.9)$$

where

$$R(q) = \begin{bmatrix} 1 - 2(q_2^2 + q_3^2) & 2(q_1 q_2 + q_0 q_3) & 2(q_1 q_3 - q_0 q_2) \\ 2(q_1 q_2 - q_0 q_3) & 1 - 2(q_1^2 + q_3^2) & 2(q_2 q_3 + q_0 q_1) \\ 2(q_1 q_3 + q_0 q_2) & 2(q_2 q_3 - q_0 q_1) & 1 - 2(q_1^2 + q_2^2) \end{bmatrix}. \quad (2.10)$$

Figure 2.3 illustrates the rotation of a vector v along the x-axis by 120 degrees about the unit vector \hat{n} . The unit vector \hat{n} represents the Euler axis and it is given by $\begin{bmatrix} 1/\sqrt{3} & 1/\sqrt{3} & 1/\sqrt{3} \end{bmatrix}^T$. Using equation (2.5), the unit quaternion can be calculated and it is given by $\begin{bmatrix} 1/2 & 1/2 & 1/2 & 1/2 \end{bmatrix}^T$. As can be seen, a rotation of 120 degrees about the referred axis moves the vector in x-axis to a new position in z-axis.

2.2.2 Modified Rodrigues Parameters

As an alternative to using quaternion representation, one can use a three-dimensional parametrization known as modified Rodrigues parameters (MRP). A MRP is defined as [5]:

$$p \equiv [p_1 \quad p_2 \quad p_3]^T = \hat{n} \cdot \tan\left(\frac{\theta_r}{4}\right), \quad (2.11)$$

where \hat{n} is the axis of rotation and θ_r is the angle of rotation. The relation between quaternions and MRPs is given by:

$$p = \frac{\vec{q}}{1 + q_0}. \quad (2.12)$$

The rotation matrix can also be defined in terms of MRP, as in

$$v^R = R(p)v, \quad (2.13)$$

where $R(p)$ is the 3x3 dimensional attitude matrix given by[5]:

$$R(p) = I_{3 \times 3} - \frac{4(1 - p^T p)}{(1 + p^T p)^2} [p \times] + \frac{8}{(1 + p^T p)^2} [p \times]^2. \quad (2.14)$$

The 3x3 dimensional matrix $[p \times]$ is referred to as cross product matrix, with

$$[p \times] = \begin{bmatrix} 0 & -p_3 & p_2 \\ p_3 & 0 & -p_1 \\ -p_2 & p_1 & 0 \end{bmatrix}. \quad (2.15)$$

2.3 The Kalman Filter

In 1960, Kalman published his famous paper with a set of mathematical equations that provide a recursive method to estimate the state of a process. The noise is assumed to be a Gaussian random process with a known covariance matrix. The filter minimizes the covariance of the estimated error between the model output and the measurements. [13].

2.3.1 The Discrete Kalman Filter

The following description of the Kalman filter is based on [26, 22]. It assumes a process model with n states. The process that is governed by the linear difference equation, in the time t_k :

$$x_{k+1} = F_k x_k + w_k, \quad (2.16)$$

where:

- x_k is the process state vector ($n \times 1$);
- F_k is the state transition matrix ($n \times n$), relating the states x_k to x_{k+1} ;
- w_k is the white process noise vector ($n \times 1$), with known covariance. $E[w_k] = 0$ and $E[w_k w_i^T] = Q_k$ if $i = k$, zero otherwise.

For a system with m outputs, the measurement equation is:

$$z_k = H_k x_k + \varepsilon_k, \quad (2.17)$$

where:

- z_k is the measurement vector ($m \times 1$);
- H_k is a $m \times n$ matrix relating the states x_k to the measurement z_k ;
- ε_k is the white measurement noise vector ($m \times 1$), with known covariance. $E[\varepsilon_k] = 0$ and $E[\varepsilon_k \varepsilon_i^T] = R_k$ if $i = k$, zero otherwise.

Both noises are assumed to be uncorrelated, or $E[w_k \varepsilon_i^T] = 0$ for all k, i .

We define \hat{x}_k^- and \hat{x}_k to be the a priori and the a posteriori state estimates respectively. The errors of the estimations are:

$$e_k^- = x_k - \hat{x}_k^-, \quad e_k = x_k - \hat{x}_k. \quad (2.18)$$

Therefore, the associated error covariance matrices are:

$$P_k^- = E[e_k^- e_k^{-T}], \quad P_k = E[e_k e_k^T]. \quad (2.19)$$

We begin with the goal of finding an equation that computes a state estimate as a linear combination of an a priori estimate and a weighted difference between an actual measurement and a measurement prediction as shown below in equation 2.20.

$$\hat{x}_k = \hat{x}_k^- + K_k (z_k - H_k \hat{x}_k^-). \quad (2.20)$$

The $z_k - H_k \hat{x}_k^-$ term is called measurement innovation and reflects the discrepancy between the predicted measurement $H_k \hat{x}_k^-$ and the actual measurement z_k . The $n \times m$ matrix K_k is the Kalman gain.

It is calculated such that it minimizes the trace of the error covariance P_k and it is given by equation (2.21). More details can be obtained from [2] and [22].

$$K_k = P_k^- H_k^T (H_k P_k^- H_k^T + R_k)^{-1}. \quad (2.21)$$

For updated estimate of the state \hat{x}_k , a new covariance matrix can be computed

$$P_k = (I - K_k H_k) P_k^-. \quad (2.22)$$

The updated estimate \hat{x}_k is then projected ahead using the process equation (2.16):

$$\hat{x}_{k+1}^- = F_k \hat{x}_k. \quad (2.23)$$

Finally, the covariance matrix for the projected state expression can be obtained using some equation substitution, as showed in [2, 22]. The result is that the projected covariance matrix is calculated as:

$$P_{k+1}^- = F_k P_k F_k^T + Q_k. \quad (2.24)$$

In many cases, the estimation begins without any prior measurements. Thus, in this case, the initial estimate of the state is usually the predicted mean and the associated error covariance matrix is just the covariance matrix of x itself [2].

Figure (2.4) offers a complete view of the filter, resuming all the operations above.

2.3.2 The Discrete Extended Kalman Filter

The extended Kalman filter or EKF is used when the process to be estimated and (or) the measurement relationship to the process is non-linear. The basic difference is that the EKF linearizes the estimation around the current estimate using the partial derivatives of the process and measurement functions. The following reasoning is also based on [22, 26].

The process has a state vector ($n \times 1$) which is now governed by the non-linear stochastic difference equation

$$x_{k+1} = f(x_k, w_k), \quad (2.25)$$

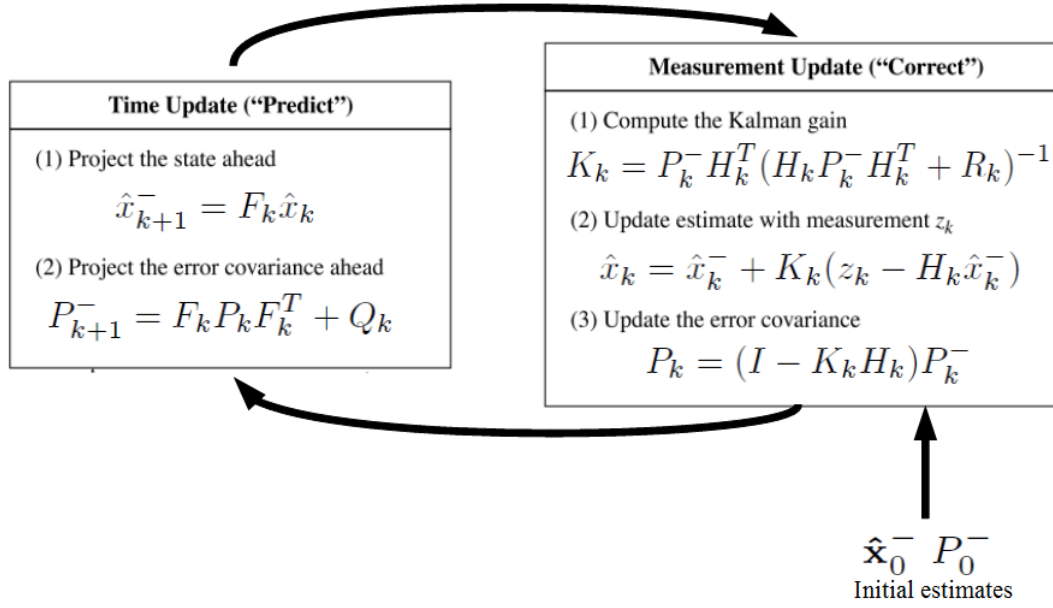


Figure 2.4: Diagram with the operations of the discrete Kalman filter. Adapted from [26].

with a measurement vector ($m \times 1$) that is

$$z_k = h(x_k, \varepsilon_k), \quad (2.26)$$

where:

- the random variables w_k and ε_k are the same random variables as in equations (2.16) and (2.17), with probability distributions $p(w_k) \sim N(0, Q_k)$ and $p(\varepsilon_k) \sim N(0, R_k)$;
- f is the non-linear function that relates the states x_k to the states x_{k+1} ;
- h is the non-linear function that relates the states x_k to the measurements z_k .

The EKF works similarly as the previous one. However, in order to estimate a process and/or measurements with non-linear difference equations, it is necessary to first linearize the equations. This is done by computing the following partial derivative matrices evaluated at the current state estimate \hat{x}_k :

$$\begin{cases} F_k = \frac{\delta f}{\delta x}(\hat{x}_k, 0), \\ W_k = \frac{\delta f}{\delta w}(\hat{x}_k, 0), \\ H_k = \frac{\delta h}{\delta x}(\hat{x}_k, 0), \\ V_k = \frac{\delta h}{\delta \eta}(\hat{x}_k, 0), \end{cases} \quad (2.27)$$

where:

- F_k is the Jacobian matrix of partial derivatives of f with respect to x ;
- W_k is the Jacobian matrix of partial derivatives of f with respect to w ;
- H_k is the Jacobian matrix of partial derivatives of h with respect to x ;
- V_k is the Jacobian matrix of partial derivatives of h with respect to ε .

To compute the prior state estimate, equation (2.25) is used as in:

$$\hat{x}_{k+1}^- = f(\hat{x}_k, 0). \quad (2.28)$$

The a priori covariance matrix is given by:

$$P_{k+1}^- = F_k P_k F_k^T + W_k Q_k W_k^T. \quad (2.29)$$

For the initial conditions, one can start with $\hat{x}_0 = E[x_0]$ and with $P_0 = E[(x_0 - \hat{x}_0)(x_0 - \hat{x}_0)^T]$.

Then, the estimation is complete by executing the following EKF measurement update equations:

$$K_k = P_k^- H_k^T (H_k P_k^- H_k^T + V_k R_k V_k^T)^{-1} \quad (2.30)$$

$$\hat{x}_k = \hat{x}_k^- + K_k (z_k - h(\hat{x}_k^-, 0)) \quad (2.31)$$

$$P_k = (I - K_k H_k) P_k^- \quad (2.32)$$

Figure 2.5 resumes the EKF operations and give a complete picture.[22] and [26] presents more details about the EKF equations. In this thesis, an extended Kalman filter is proposed for attitude determination and, therefore, the equations presented previously are used throughout the thesis.

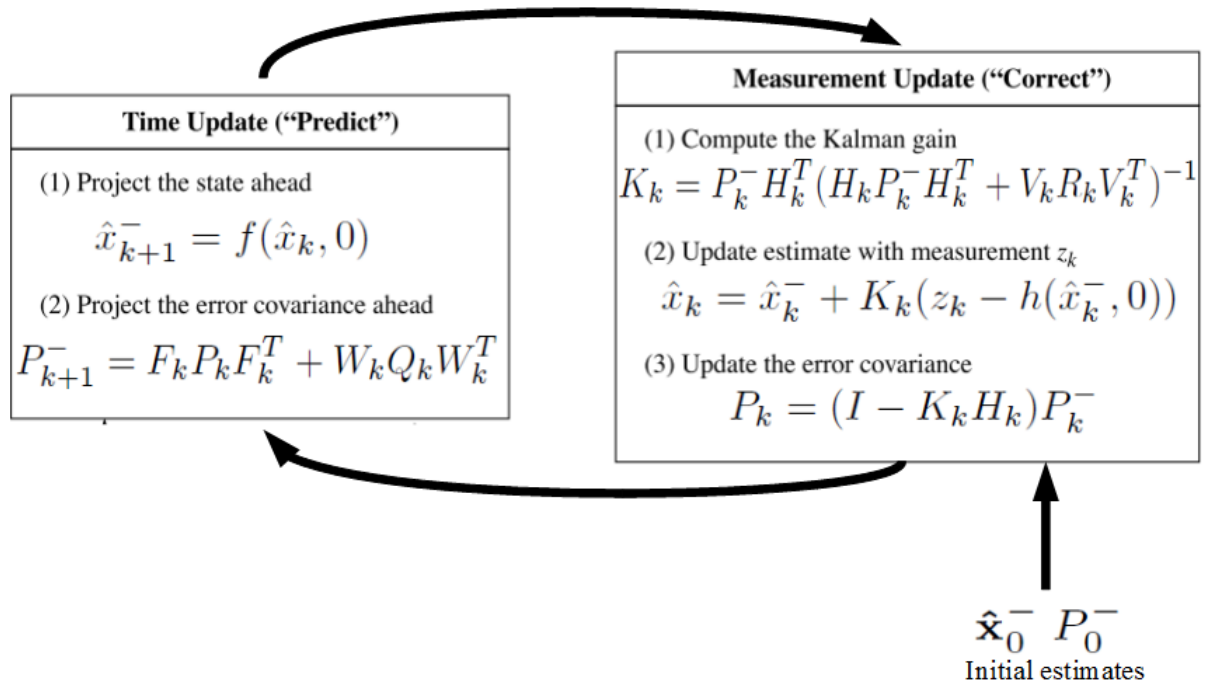


Figure 2.5: Diagram with the operations of the extended Kalman filter. Adapted from [26].

Chapter 3

Calibration

An inertial measurement unit consists of a cluster of sensors used to determine the attitude of a body in three dimensional space. Development in micro-electro-mechanical system (MEMS) technology has made it possible to fabricate low cost IMUs, with the drawback of reduced accuracy than the traditional inertial measurement units. Therefore, calibration procedures must be performed to correct the sensor readings to achieve precise attitude reconstruction.

The following IMUs are used in this project:

1. 3DM-GX3-25 from MicroStrain Sensors, shown in 3.1 (a).
2. MinIMU-9 v2 from Pololu, shown in 3.1 (b).

Both of them comprises three accelerometers, three angular rate sensors, and three magnetometers.

The inertial sensor errors can be divided into two parts: deterministic and stochastic. The deterministic error sources include the bias, the scale factors, and the misalignment errors which can be determined by a calibration procedure, discussed in this chapter. The stochastic part contains random

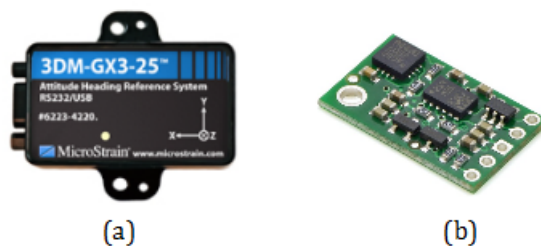


Figure 3.1: Pictures of the IMUs used in the project.

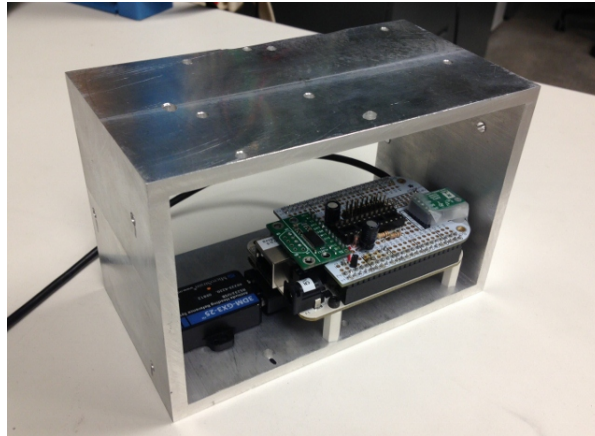


Figure 3.2: IMUs mounted in a aluminum structure.

errors (noises) which cannot be removed from the measurements and should be modeled as stochastic processes. The Allan Variance method is applied in determining those sources of errors. Chapter 4 will discuss the Allan variance method and the sensor random errors.

The first IMU (MicroStrain's 3DM-GX3-25) has already been calibrated from factory. According to the vendors datasheet [31], the calibration was performed over the temperature range of the sensor and the calibration coefficients were written on the sensors non-volatile memory. These coefficients are used by the algorithm during operation to correct the measurements, eliminating common sources of error such as hysteresis induced by temperature changes and sensitivity to supply voltage variations. Gyro drift is reduced by referencing magnetic North and Earth's gravity and compensating for gyro bias.

On the other hand, the second IMU (Pololu's MinIMU-9 v2) needs to be calibrated, since no signal processing was performed from the factory, and the procedure is discussed in this chapter. This IMU has the advantage to be cheaper with the drawback to have worse noise characteristics.

Since the simulation table was in design phase when this thesis was written, the IMUs were mounted in a rectangular aluminum structure, exhibited in figure 3.2. Aluminum extrusions are very straight and square, making it ideal for the calibration procedure and Kalman filter tests. The sensing coordinate frames from both sensors were aligned so that they would provide the same readings. The MicroStrain IMU was fixed directly to the structure (as seen on the left) while the Pololu IMU was connected to the Beagle Bone, which was screwed in the aluminum frame (on the right).

3.1 Calibration Concept

The calibration is done by turning the IMU into different precisely controlled orientations and at known rotational velocities [11].

- For the gyros, the calibration is done using air bearing table equipped with a high precision encoder. The encoder is used to give the true angular rates.
- For the accelerometer, the known gravity field of the Earth is going to be used to produce known accelerations. The sensors are placed into a leveled platform to ensure perfect alignment with gravitational vector.

At each configuration, a set of samples is taken for each sensor after waiting for it to settle. Based on these measurements, the optimal parameters of the sensor model are calculated using a least squares algorithm.

For the magnetometer, the ellipsoid fit algorithm is used. It is discussed in detail in section 3.4.

3.2 Sensor Error Model

In this section, the deterministic part of the error is going to be detailed and a sensor error model is going to be obtained. The procedure was taken from [18, 23].

The sensor model describes the process of measurement from the actual physical quantity to the sensor voltage output.

3.2.1 Scale factor

The first instrumentation error corresponds to constants of proportionality relating the input to the output. The scale factor matrix can be defined as

$$K_{scale} = \begin{bmatrix} k_x & 0 & 0 \\ 0 & k_y & 0 \\ 0 & 0 & k_z \end{bmatrix}, \quad (3.1)$$

where k_i is the scaling of the output of the sensor's i -th sensitivity axis.

3.2.2 Bias

There is often a small bias in the sensor output signal, defined as

$$b = \begin{bmatrix} b_x & b_y & b_z \end{bmatrix}^T, \quad (3.2)$$

where b_i is the bias of the output of the sensor's i -th sensitivity axis.

3.2.3 Non-orthogonality

The non-orthogonal sensor sensitivity axes differ to the orthogonal body frame coordinate axes of the IMU due to fabrication limitations, as shown in figure 3.3. This difference is only by "small" angles. The measurements, collected in sensitivity coordinates, can be transformed into measurements in body frame coordinates following the relation:

$$s^B = T_S^B s^S, \quad T_S^B = \begin{bmatrix} 1 & -\alpha_{yz} & \alpha_{zy} \\ \alpha_{xz} & 1 & -\alpha_{zx} \\ -\alpha_{xy} & \alpha_{yz} & 1 \end{bmatrix}, \quad (3.3)$$

where s^B and s^S denote the measurement in body frame coordinates and IMU sensitivity coordinates, respectively. The angles α_{ij} represents the rotation of the i -th sensor sensitivity axis around the j -th body frame axis, see figure 3.3.

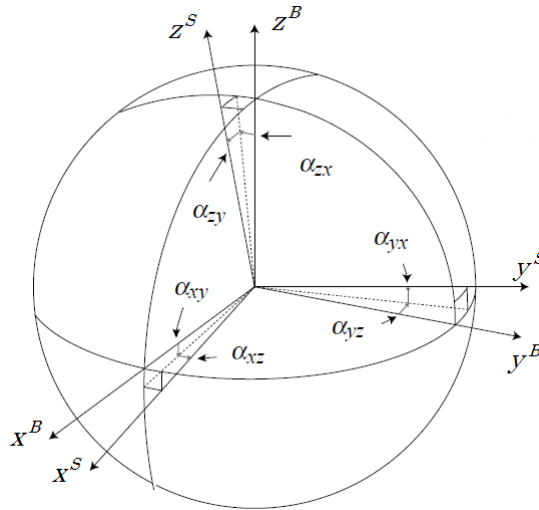


Figure 3.3: Sensor (accelerometer, gyroscope or magnetometer) sensitivity axes $[x^S \ y^S \ z^S]^T$ and body frame coordinate axes $[x^B \ y^B \ z^B]^T$. From [23].

3.2.4 Sensor Error Model Equation

Using $s^S = (T_S^B)^{-1} s^B$ from equation (3.3), the sensor error model equation is

$$v^M = K_{scale} s^S + b = K_{scale} (T_S^B)^{-1} s^B + b \quad (3.4)$$

where v^M is the voltage measured from the sensor. The described sensor error model uses a total of twelve parameters: three for scale errors, three for bias errors and six for misalignment and non-orthogonality errors.

The equation (3.4) can be rewritten to get the body frame coordinate axis measurements as a function from the sensor voltage output:

$$s^B = T_S^B (K_{scale})^{-1} (v^M - b) \quad (3.5)$$

or simplifying in a matrix form

$$\begin{bmatrix} x^B \\ y^B \\ z^B \end{bmatrix} = \begin{bmatrix} T_S^B (K_{scale})^{-1} & -T_S^B (K_{scale})^{-1} b \end{bmatrix} \begin{bmatrix} v_x^M \\ v_y^M \\ v_z^M \\ 1 \end{bmatrix}. \quad (3.6)$$

3.3 Calibration Algorithm

The mechanical calibration table and the high precision instruments are used to provide accurate values for the triad s^B , which will be the reference value. Defining the matrix C as

$$C = \begin{bmatrix} T_S^B (K_{scale})^{-1} & -T_S^B (K_{scale})^{-1} b \end{bmatrix} = \begin{bmatrix} c_1 & c_2 & c_3 & c_4 \\ c_5 & c_6 & c_7 & c_8 \\ c_9 & c_{10} & c_{11} & c_{12} \end{bmatrix}, \quad (3.7)$$

it has the 12 calibration parameters to be determined [18]. Having the values of s^B provided by the calibration table and measuring the digital output values v^M from the sensor, the 12 calibration parameters values can be obtained.

The obvious choice to solve this problem is a linear least squares approach. The parameters can be written in the vector form as $c = [c_1 \dots c_{12}]^T$. Therefore, equation (3.6) can be rewritten as

$$\begin{bmatrix} x^B \\ y^B \\ z^B \end{bmatrix} = \begin{bmatrix} v_x^M & v_y^M & v_z^M & 1 & 0 & 0 & 0 & 0 & 0 & 0 & 0 & 0 \\ 0 & 0 & 0 & 0 & v_x^M & v_y^M & v_z^M & 1 & 0 & 0 & 0 & 0 \\ 0 & 0 & 0 & 0 & 0 & 0 & 0 & 0 & v_x^M & v_y^M & v_z^M & 1 \end{bmatrix} c \quad (3.8)$$

$$s^B = Yc.$$

The matrix Y and the the vector s^B grow vertically when more measurements are considered in the calculation. Finally, [18]:

$$c = (Y^T Y)^{-1} Y^T s^B. \quad (3.9)$$

The calibration vector c suffices as an output as the measurement in the body frame axis can be obtained from the relation

$$\begin{bmatrix} x^B \\ y^B \\ z^B \end{bmatrix} = \begin{bmatrix} c_1 & c_2 & c_3 \\ c_5 & c_6 & c_7 \\ c_9 & c_{10} & c_{11} \end{bmatrix} \begin{bmatrix} v_x^M \\ v_y^M \\ v_z^M \end{bmatrix} + \begin{bmatrix} c_4 \\ c_8 \\ c_{12} \end{bmatrix}. \quad (3.10)$$

3.4 The Magnetometer Case

Apart from the errors considered in section 3.2, the magnetometers also suffer from magnetic deviations which can be caused by hard iron or soft iron effects. Hard iron effects are due to the permanent magnetization of the sensor and lead to a constant additional magnetic field equivalent to a bias [19]:

$$b_{hi} = [b_{hi_x} b_{hi_y} b_{hi_z}]. \quad (3.11)$$

Soft iron effects are due to magnetization of the sensor as a result of an external magnetic field and will therefore depend on the orientation of the sensor with respect to the external field. It can change both the intensity and the direction of the sensed field. Soft iron effect can be modeled as a 3 by 3 matrix named C_{si} [19]. Extending equation (3.4) to also include the model of the magnetic disturbances introduced above, results in

$$v^M = K_{scale} (T_S^B)^{-1} C_{si} s^B + b + b_{hi}. \quad (3.12)$$

This hard and soft iron effects are introduced externally by mounting structures or adjacent devices, such as ferrous metal structures and mounting components (steel nuts and bolts), which are are hard

to avoid. Since both IMUs were mounted in a aluminum frame, the hard and soft iron effects will be absolutely present and, consequently, the calibration of the magnetometer of both sensors must be performed. Also, after the installation of the IMUs in the satellite simulator structure (in the future), the calibration of the magnetometer of both sensors must be performed again, considering that soft and hard iron effects will be certainly present.

We assume that all magnetic disturbances present are stationary and constant, i.e. rigidly attached to the sensor. Also, the local magnetic field is assumed constant, as the calibration was performed in one room.

It is possible to simplify equation (3.12) defining a calibration coefficient matrix C for the magnetometer case, which is:

$$C = \begin{bmatrix} C_{si}^{-1} T_S^B (K_{scale})^{-1} & -C_{si}^{-1} T_S^B (K_{scale})^{-1} (b + b_{hi}) \end{bmatrix} = \begin{bmatrix} c_1 & c_2 & c_3 & c_4 \\ c_5 & c_6 & c_7 & c_8 \\ c_9 & c_{10} & c_{11} & c_{12} \end{bmatrix} \quad (3.13)$$

Hence, equation (3.12) can be rewritten in a simpler form as in equation (3.10):

$$\begin{bmatrix} x^B \\ y^B \\ z^B \end{bmatrix} = \begin{bmatrix} c_1 & c_2 & c_3 \\ c_5 & c_6 & c_7 \\ c_9 & c_{10} & c_{11} \end{bmatrix} \begin{bmatrix} v_x^M \\ v_y^M \\ v_z^M \end{bmatrix} + \begin{bmatrix} c_4 \\ c_8 \\ c_{12} \end{bmatrix} \quad (3.14)$$

Next section aims to describe how to obtain the coefficients from c_1 to c_{12} .

3.4.1 Magnetometer Calibration Algorithm

The norm of the magnetometer vector measurement should be equal to the magnitude of the Earth's magnetic field. Consequently, while rotating the sensor in space, the locus described by its readings should describe a sphere with a radius equal to the magnitude of the local Earth's magnetic field. Given that the points s^B are contained in a sphere, it is straightforward to show that the magnetometer readings v^M lie on an ellipsoid manifold, as illustrated in figure 3.4 and explained in detail in [14, 19, 24].

For a properly calibrated magnetometer, the magnitude of the measured magnetic field is not dependent on the orientation of the sensor, implying that the collected magnetometer data lies on a sphere. The presence of magnetic distortions leads to errors which cause the magnetometer data to lie on an ellipsoid instead. Calibrating a tri-axis magnetometer is equivalent to the estimation of the ellipsoid's parameters.

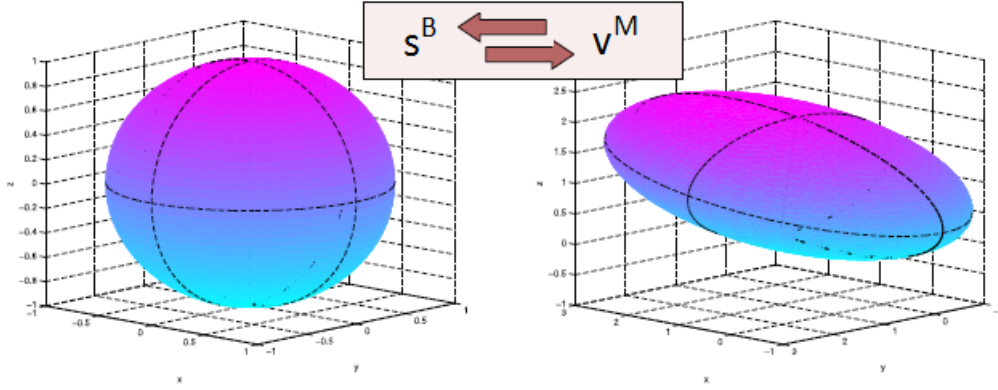


Figure 3.4: Ellipsoid data leads to calibrated measurements lying on the sphere. From [24].

Using magnetic field measurements collected in a perturbation free environment while rotation the sensor along several orientations, it is possible to map the ellipsoid to a sphere. Using the least squares algorithm, a transformation matrix and a offset vector necessary to fit the magnetometer data ellipsoid into a sphere are calculated. From there, the calibration elements c in (3.14) are derived, where:

- Transformation matrix =
$$\begin{bmatrix} c_1 & c_2 & c_3 \\ c_5 & c_6 & c_7 \\ c_9 & c_{10} & c_{11} \end{bmatrix};$$

- Offset vector =
$$\begin{bmatrix} c_4 \\ c_8 \\ c_{12} \end{bmatrix}.$$

3.5 Procedures and Results

The algorithms described in the previous sections are performed offline using measurements acquired from both IMUs and reference encoder. The diagram in figure 3.5 presents how the instruments are connected with a computer, used for data analysis.

A Labview routine is used to collect data from the high precision encoder, which measures the angular position in the single axis air bearing, and store it into a spreadsheet (.csv file) saved directly in the computer. On the other hand, the data from the MicroStrain and Pololu IMUs is stored in the Beagle Bone into another .csv file. At the end of the procedure, the data is downloaded in the computer.

Although the MicroStrain IMU was calibrated in the factory, misalignment in the mounting of the sensor in the aluminum structure may still exist and it is useful/important to estimate the error. There-

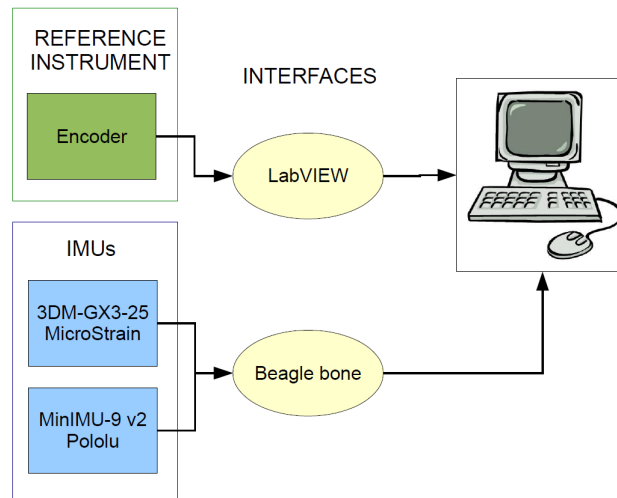


Figure 3.5: Diagram with the IMUs, the encoder, and its interfaces with the computer

fore, it was decided to calibrate not only its magnetometers, but also its accelerometers and gyros to ensure that the both sensors are in perfect alignment with the aluminum structure.

The IMUs were powered approximately 1 hour before the procedures to allow them to “warm-up”. There is an immediate increase in the IMU’s temperature after the power is on, caused by a heating of the internal components when the power is applied to the electrical circuits. The self-heating effect results in an initial transient of a few minutes before the outputs are thermally stabilized [20]. The transient effect is not desirable while calibrating and, hence it was avoided by heating up the IMUs before the experiments.

The following sections describe the procedures adopted to calibrate the accelerometers, gyros and magnetometers followed by a section with the results.

3.5.1 Accelerometer

The earth gravity is used to calibrate the accelerometers. This method requires the IMU to be mounted on a leveled platform with each sensitive axis pointing alternately in different positions[11]. The leveled platform used for the procedures is presented in figure 3.6. It was placed on the ground to minimize extraneous motion and vibration. The platform is made from machined and polished granite, with a very smooth flat surface. It has three mounting holes in a triangular shape, defining a stable plane (no wobbling). At each corner is a thumb screw for leveling. A bubble level with 0.2 mm precision was placed on the platform to check its orientation and the screws were adjusted until the platform was leveled.

The cubic structure with the IMUs and the Beagle Bone was placed on the leveled platform in 6

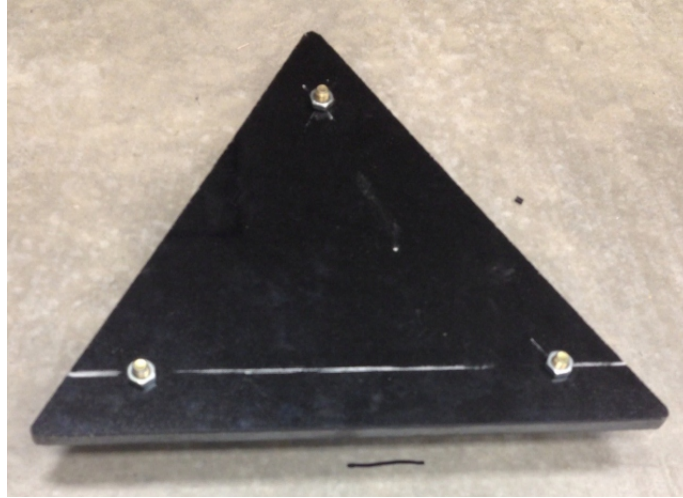


Figure 3.6: Leveled platform used to calibrate the accelerometers.

different positions, indicated in figure (3.7).

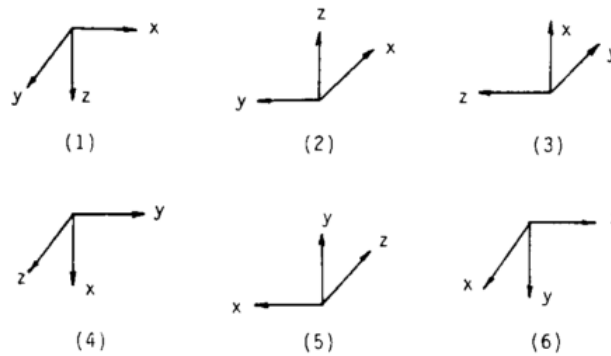


Figure 3.7: 6 positions of the accelerometer calibration. From [11].

The measured quantity v^M is the gravity as sensed by the sensors. The reference value s^B is the known value of gravity in each configuration. For example, in the position (2) of figure 3.7, $s^B = [0 \ 0 \ -g]$.

At each position, the “cube” is left at rest for approximately 10 seconds. Using a sample frequency of 50 Hz, about 500 measurements are made in each position. After rotating through all six positions, the data recorder was turned off and the measurements were saved.

Figures 3.8 and 3.9 show the comparison between the reference output in blue and the sensor output in red for the Pololu and MicroStrain IMUs respectively.

Using the least squares algorithm described previously in section 3.3, the calibration matrix was calculated for each IMU. Using the reference values in the s^B vector and the measured value to form the matrix Y , the results obtained were (the uppercase indicates the IMU - Pol for Pololu and MS for MicroStrain):

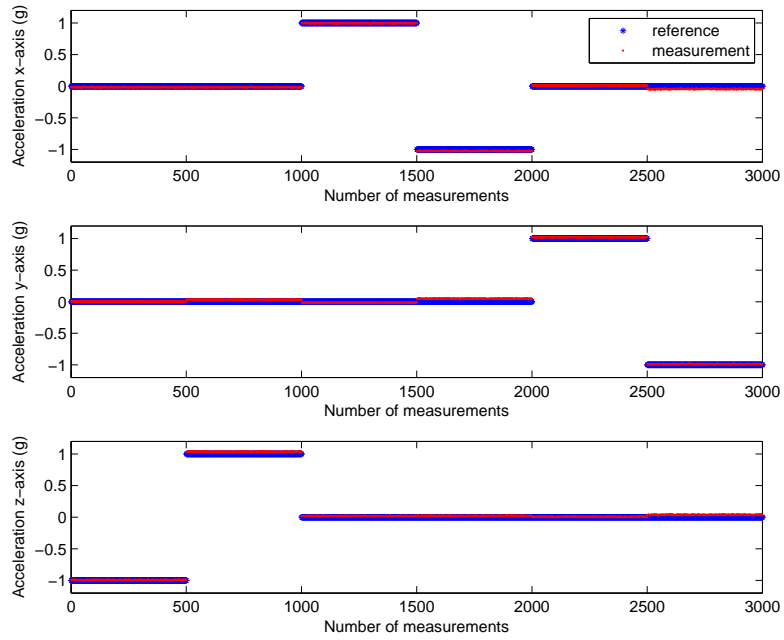


Figure 3.8: Accelerometer calibration of the Pololu IMU.

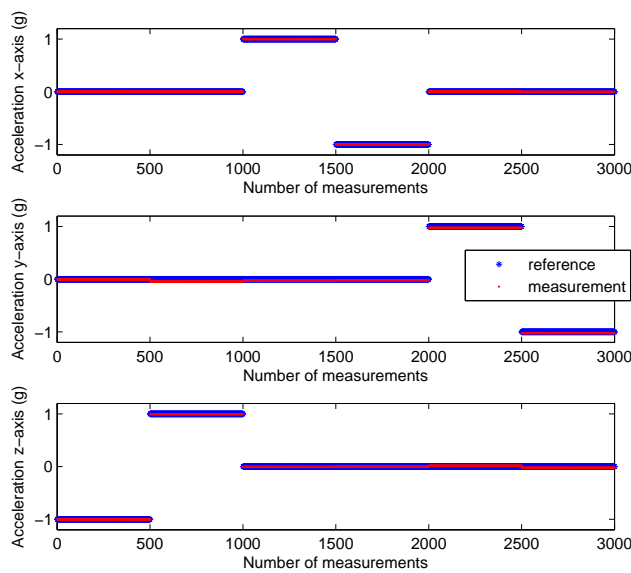


Figure 3.9: Accelerometer calibration of the MicroStrain IMU.

$$C_{acc}^{Pol} = \begin{bmatrix} 0.9891 & -0.0144 & 0.0063 & 0.0118 \\ 0.0268 & 0.9943 & 0.0012 & -0.0147 \\ -0.0048 & 0.0001 & 0.9869 & -0.0201 \end{bmatrix},$$

$$C_{acc}^{MS} = \begin{bmatrix} 1.0009 & 0.0079 & 0.0002 & -0.0062 \\ 0.0050 & 1.0007 & 0.0191 & 0.0239 \\ 0.0026 & -0.0185 & 1.0009 & 0.0027 \end{bmatrix}.$$

These matrices have the 12 calibration parameters defined in equation (3.7). They are used to obtain the calibrated measurements, as evidenced in equation (3.10).

3.5.2 Gyroscope

The angular rate measurements are taken by rotating the IMUs around its body frame axes x , y and z (one at a time) in an air bearing table equipped with a high precision encoder, shown in figure 3.10. The encoder provides the angular position used as reference for the calibration. The encoder has a resolution of 15.82 arc-sec/count or 81,920 counts per revolution.

The air bearing table was placed over the leveled platform and the “cube” with the IMUs and Beagle Bone was screwed on the top of the air bearing using the mounting holes. First, the table was rotated about the z axis followed by the y axis and x axis. The rotation was performed by manually turning the aluminum cube with random angular rates.

The measured quantity ν^M is the angular velocity read from the IMUs. The reference value s^B is the angular rate derived from the precise angular position measured by the encoder. In order to obtain precise angular rates, it was necessary to record accurate time stamps of the measurements. Data was acquired at a frequency of 50 Hz. 20 seconds of data in each configuration were used to obtain the calibration matrix C .

The plots in figures 3.11 and 3.12 presents the reference and measured quantities for both IMUs. The results of the least square algorithm to calculate the calibration parameters are:

$$C_{gyro}^{MS} = \begin{bmatrix} 1.0000 & 0.0260 & 0.0028 & 0.0001 \\ -0.0040 & 0.9994 & 0.0261 & 0.0001 \\ 0.0260 & -0.0034 & 0.9990 & 0.0004 \end{bmatrix};$$



Figure 3.10: Air bearing table.

$$C_{gyro}^{Pol} = \begin{bmatrix} 1.0348 & 0.0043 & -0.0196 & -0.0038 \\ 0.0509 & 1.0249 & 0.0297 & -0.0098 \\ -0.0416 & 0.0172 & 1.0386 & -0.0188 \end{bmatrix}.$$

3.5.3 Magnetometer

The magnetometer calibration must be performed every time a new configuration of the assembly is made. This is due to the hard and soft iron effects that change the magnetic field readings every time ferrous materials are placed in a new position with respect to the IMUs. Therefore, the magnetometer was calibrated several times.

The calibration test presented in this work was performed before the Kalman filter testing. The aluminum cube with the IMUs was rigidly attached to the air bearing table with the z-axis pointing up. The whole structure was rotated in the 3D space in random paths while the data was collected with a frequency of 5 Hz (10 times slower than the other tests). The calibration consists of fitting those magnetometer's field measurements on the sphere manifold.

Figure 3.13 depicts the measurements from both sensors before and after the calibration, in red and blue respectively. The following matrices give the calibration parameters computed with the proposed algorithm.

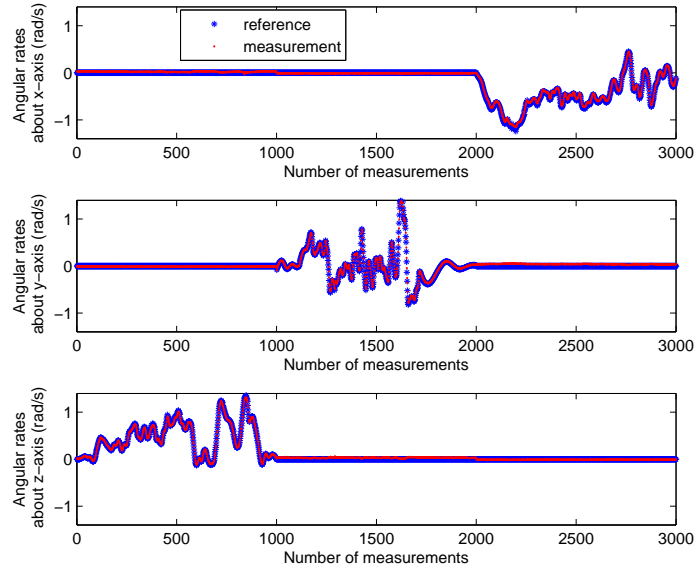


Figure 3.11: Gyroscope calibration of the Pololu IMU.

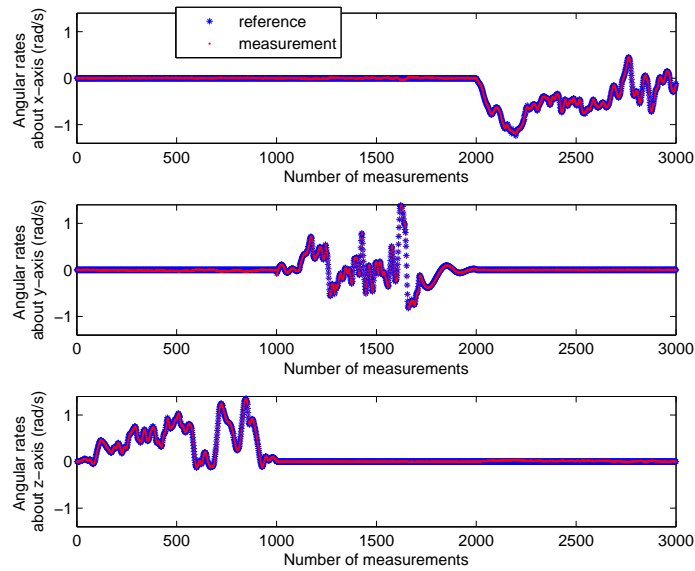


Figure 3.12: Gyroscope calibration of the MicroStrain IMU.

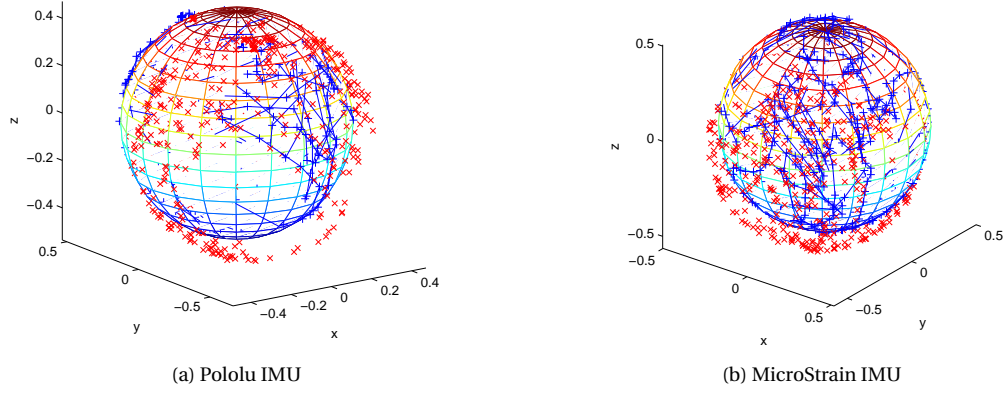


Figure 3.13: Magnetometer calibration results, in Gauss. Non-calibrated magnetic field measurements in red and calibrated magnetic field measurements in blue.

$$C_{mag}^{Pol} = \begin{bmatrix} 0.9905 & 0.0075 & 0.0064 & -0.0142 \\ 0.0075 & 1.0694 & 0.0127 & -0.1145 \\ 0.0064 & 0.0127 & 0.9481 & -0.0293 \end{bmatrix},$$

$$C_{mag}^{MS} = \begin{bmatrix} 1.0128 & -0.0090 & -0.0019 & 0.0904 \\ -0.0090 & 0.9868 & 0.0061 & 0.0813 \\ -0.0019 & 0.0061 & 1.0012 & 0.0354 \end{bmatrix}$$

Chapter 4

Sensor Noise Model

In this chapter, a simple but realistic sensor noise model is developed. The Allan variance method is used, based on the IEEE STD 647-2006 [30]. Several authors use the Allan variance method to characterize error sources of inertial sensors as in [9, 8, 29] and specially [10], which served as a guide to the procedure described in this chapter.

4.1 Sensor Noise Model Equation

A widely used model for the sensors noise is given by [16]:

$$\tilde{y} = y_{\text{true}} + \beta + \eta_w \quad (4.1)$$

where:

- \tilde{y} is the measured signal, which can be acceleration, angular rates or magnetic field intensity depending of the sensor;
- y_{true} is the true value of the measured signal;
- β is the bias due to random error or drift-rate bias;
- η_w is the Gaussian white-noise with mean zero and variance given by σ_w^2 .

The drift-rate bias is not static, it can be modeled as a first order Gauss-Markov process representing exponentially correlated noise, as shown in equation (4.2) [9, 29]:

$$\dot{\beta} = -\frac{\beta}{\tau_b} + \eta_b \quad (4.2)$$

where:

- τ_b is the correlation time
- η_b is the Gaussian white-noise with mean zero and variance given by σ_b^2 .

The discrete time model of the drift-rate bias noise is:

$$\beta(k+1) = A_d\beta(k) + B_d\eta_b \quad (4.3)$$

where:

- $A_d = \exp(-\frac{\Delta t_s}{\tau_b})$
- $B_d = \int_0^{\Delta t_s} \exp(-\frac{\tau}{\tau_b}) d\tau$
- Δt_s is the sample time.

4.2 Allan Variance Definition

Allan variance is a method of analysis in a time domain. It describes the variance of a measured quantity as a function of the average time. It can be calculated using the following relation[29]:

$$\sigma_y^2(\tau) = \frac{1}{2(M-1)} \sum_{i=1}^{M-1} (\bar{y}_{i+1} - \bar{y}_i)^2 \quad (4.4)$$

where:

- M represents the number of clusters in the data set;
- τ is the time length of the cluster in seconds;
- y_i is the mean value of the cluster i .

Figure 4.1 illustrates an example of how to obtain the Allan variance parameters using a data set with 12 samples and sample time of 0.1 s.

Frequently, the Allan variance term is also used to refer to its square root, the Allan deviation $\sigma_y(\tau)$. The Allan variance method consists in analyzing the plots of the Allan deviation versus the average time

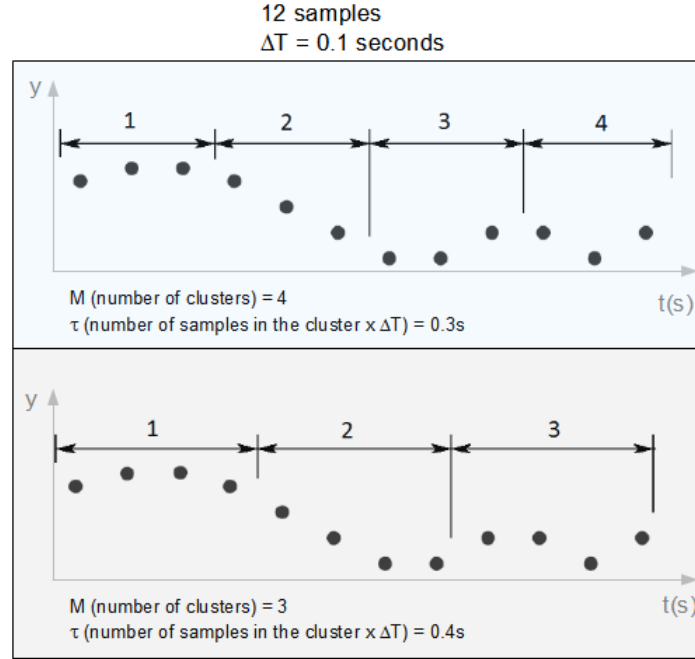


Figure 4.1: Example of the data structure used to derive Allan variance.

$[\tau \times \sigma_y(\tau)]$, on a logarithmic scale. By analyzing the plots, it is possible to identify unpredictable stochastic processes like quantization noise, angle random walk, bias instability, rate random walk or drift rate ramp, as detailed in the IEEE standard [30]. In the next section, the Allan deviation plots are presented for all the signals of both IMUs.

4.3 Allan Deviation Plots

The Allan deviation plots were obtained using data from the IMUs when kept at rest for approximately 3 hours, using the following sample times:

- MicroStrain 3DM-GX3-25: $\Delta t_s = 0.04s$ or $f = 25Hz$.
- Pololu MinIMU-9 v2: $\Delta t_s = 0.02s$ or $f = 50Hz$.

The Allan deviation plots of the accelerations, angular rates, and magnetic fields versus τ are shown in figures 4.2, 4.3 and 4.4 respectively.

Comparing the Allan deviation plots from both sensors, it is possible to verify that the MicroStrain 3DM-GX3-25 is less noisy, as the values of Allan deviation are smaller for both magnetic field and acceleration measurements. The angular rate signal of both sensor have similar noise variances, although the MicroStrain 3DM-GX3-25 have a smaller drift-bias, as explained in next section.

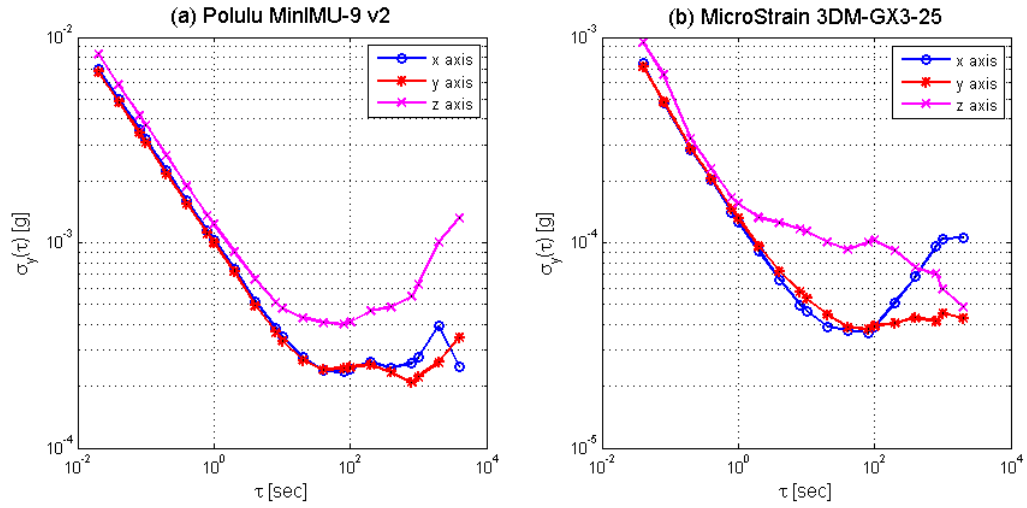


Figure 4.2: Allan deviation for the acceleration data for both IMUs.

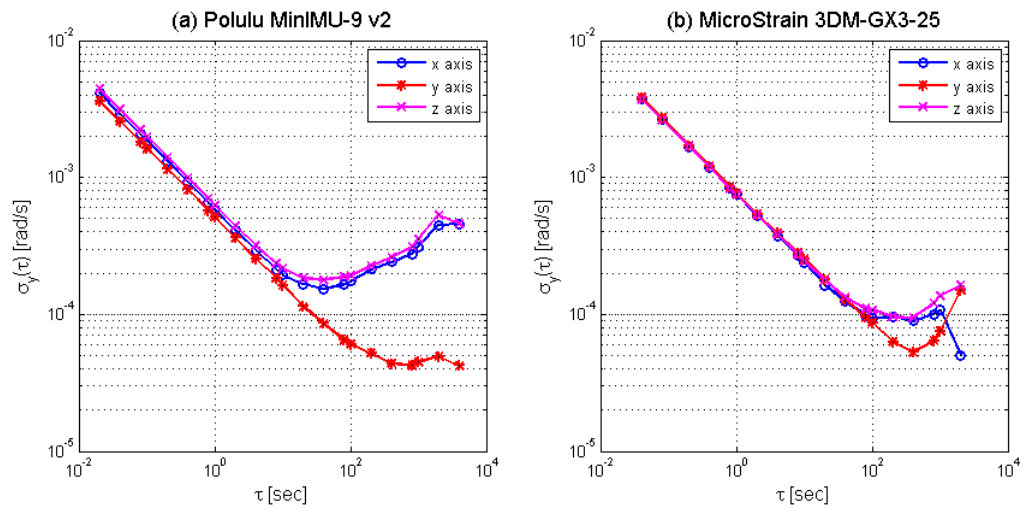


Figure 4.3: Allan deviation for the angular rate data for both IMUs.

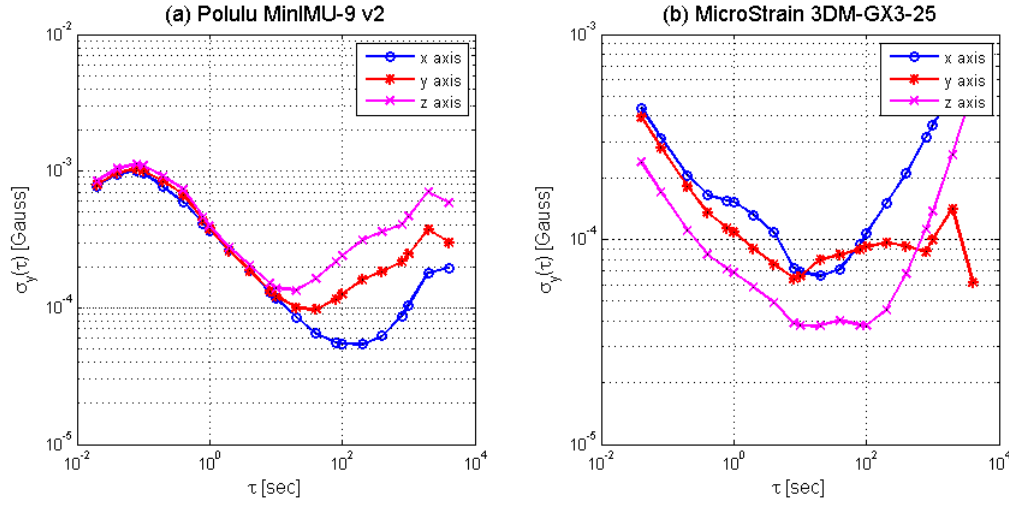


Figure 4.4: Allan deviation for the magnetic field data for both IMUs.

4.4 Noise in terms of Allan Variance

In this section, the model for the Gaussian white-noise η_w and the model for the drift-rate bias b_r (see equations 4.1 and 4.3) are going to be determined using the Allan deviation plots. In order to do that, it is assumed that the Allan deviation plots are composed only by white noise and exponentially correlated noise.

4.4.1 White Noise Part

The white noise part analysis is used to determine the value of the variance σ_w^2 of the Gaussian white-noise η_w .

Observing the graphs 4.2, 4.3, and 4.4, it is noticeable that for small values of τ the plot is a slope with inclination $-1/2$. This behavior is characteristic of the angle random walk part of the noise, which has the coefficient given by [30, 7, 10]:

$$N = \sigma_y(\tau)\sqrt{\tau} \quad (4.5)$$

where N is the angle random walk coefficient. The numerical value of N it is simply the Allan deviation value when τ is 1.

With the value of N , it is possible to calculate the Allan variance due to white noise only using equation 4.6.

$$\sigma_1^2(\tau) = \frac{N^2}{\tau} \quad (4.6)$$

where σ_1^2 is the white noise part of the Allan variance.

The variance of the white-noise η_w is simply the value of the white noise part Allan variance (σ_1^2) when τ is the sample time:

$$\sigma_w^2 = \sigma_1^2(\Delta t_s) = \frac{N^2}{\Delta t_s} \quad (4.7)$$

It is clear in equation (4.7) that the white-noise variance depends on N and on the sample time used to acquire the signals.

Subtracting the white noise part from the total Allan variance, what is left is the exponentially correlated noise part.

4.4.2 Exponentially Correlated Noise Part

The Allan deviation of the exponentially correlated noise part is given by the total Allan deviation minus the white noise part, or:

$$\sigma_2(\tau) = \sigma_y(\tau) - \sigma_1(\tau) \quad (4.8)$$

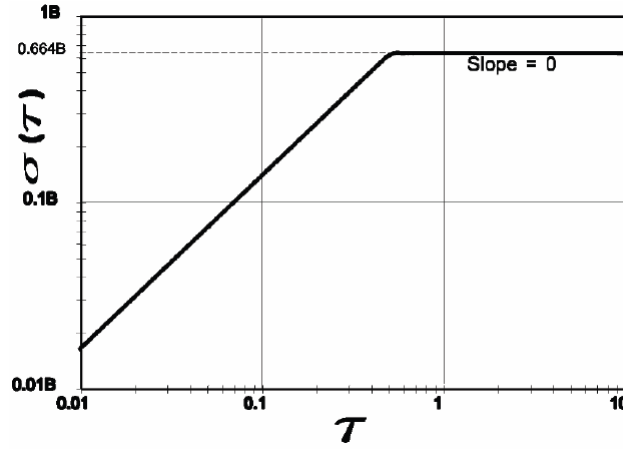
where σ_2 is the exponentially correlated noise part of the Allan deviation.

This part of the noise is described by equation (4.2). Two terms must be determined: (1) the time constant τ_b and (2) the bias variance σ_b^2 .

To obtain the time constant, it is necessary to remember that Gauss-Markov processes have an exponential auto-correlation functions. By obtaining the auto-correlation plot of the exponentially correlated noise part ($\sigma_2^2(\tau)$), the time constant can be determined by picking the value of the auto-correlation function when the curve reaches $1/e$ of its maximum value [8, 29].

To obtain the bias variance, first it is necessary to find the bias instability coefficient B [12]. According to the IEEE standard [30], the Allan variance of the bias instability noise have the log-log plot as in figure (4.5). It is seen that Allan standard deviation begins with a slope of +1 for small values of τ and reaches the asymptotic value of $0.664B$. Consequently, the value of B can be obtained by dividing the value of the Allan deviation when the slope is zero (which happens when $\tau \gg \Delta t_s$) by 0.664, as in:

$$B = \frac{\sigma_2(\tau \gg \Delta t_s)}{0.664}. \quad (4.9)$$

Figure 4.5: $\sigma(\tau)$ plot for bias instability. From [30].

For the continuous time, the bias standard deviation is simply the value of B , or $\sigma_b = B * 1s$.

Discrete-time approximation

Normally, the values of τ_b for IMU sensors are greater than 50 seconds. In those cases, one can approximate equation (4.12) with $A_d = 1$ and $B_d = \Delta t_s$, which simplifies it as:

$$\beta(k+1) = \beta(k) + \eta_{bd} \quad (4.10)$$

where η_{bd} is the discrete Gaussian white-noise with mean zero and standard deviation given by

$$\sigma_{bd} \approx B_d \sigma_b \approx \Delta t_s \sigma_b. \quad (4.11)$$

The same result can also be achieved using the discrete time variance formula, which is given by equation (4.12). For large values of τ_b , the result is also approximately $\sigma_{bd} \approx \Delta t_s \sigma_b$.

$$\sigma_{bd}^2 = \int_0^{\Delta t_s} \exp\left(-\frac{\tau}{\tau_b}\right) \sigma_b^2 \exp\left(-\frac{1}{\tau_b} \Delta t_s \tau\right) d\tau \quad (4.12)$$

4.5 Example

To illustrate the procedures, the angular rate z-axis of the MicroStrain 3DM-GX3-25 sensor is going to be used as an example. Figure 4.6 shows a plot of the actual sensor output and its Allan deviation chart.

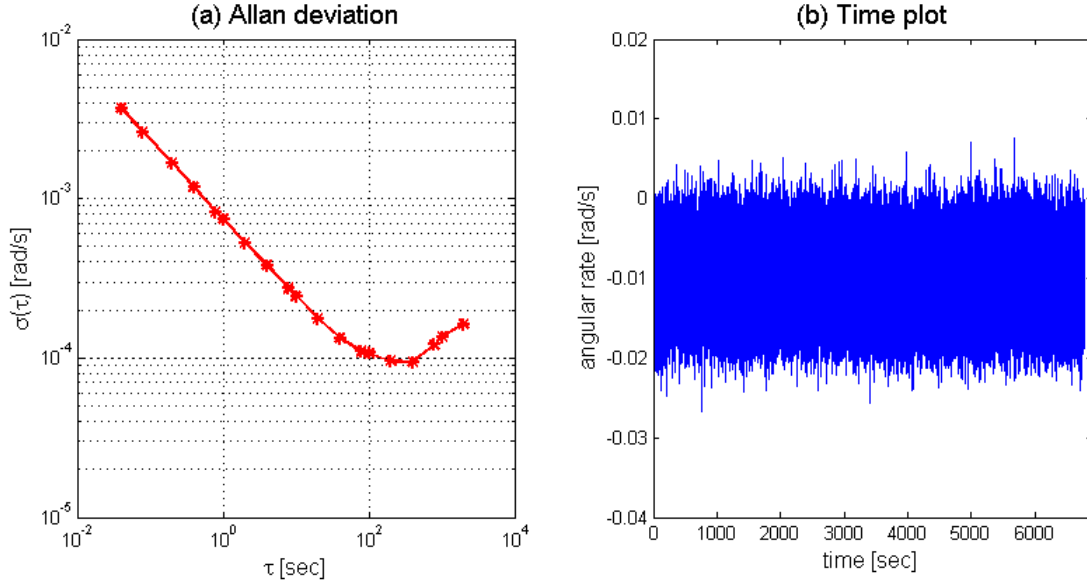


Figure 4.6: y-axis gyro output from MicroStrain 3DM-GX3-25.

4.5.1 White noise part

N is the value of Allan deviation when $\tau = 1\text{s} = 10^0\text{s}$. Therefore, $N = 7.416 \cdot 10^{-4}$. Using this information, it is possible to obtain the Allan deviation due to white noise only ($\sigma_1(\tau)$) using equation 4.6. The result is given in figure 4.7.

The deviation of the white-noise η_w is simply the value of the white noise part Allan deviation (σ_1) when τ is the sample time, given by the first value of the plot:

$$\sigma_w = \sigma_1(0.04) = 3.781 \cdot 10^{-3} \text{ rad/s} \quad (4.13)$$

4.5.2 Exponentially Correlated Noise Part

Subtracting the curves in figure 4.7, the remaining is the exponentially correlated part of the noise (σ_2). Its auto-correlation plot is shown in figure 4.8. The value of the correlation time is given by the time when the curve reaches $1/e$ of its maximum value (dashed green line). Hence:

$$\tau_b = 672\text{s}$$

Using τ_b , it is possible to obtain the values of A_d and B_d from equation (4.3). As the value of τ_b is

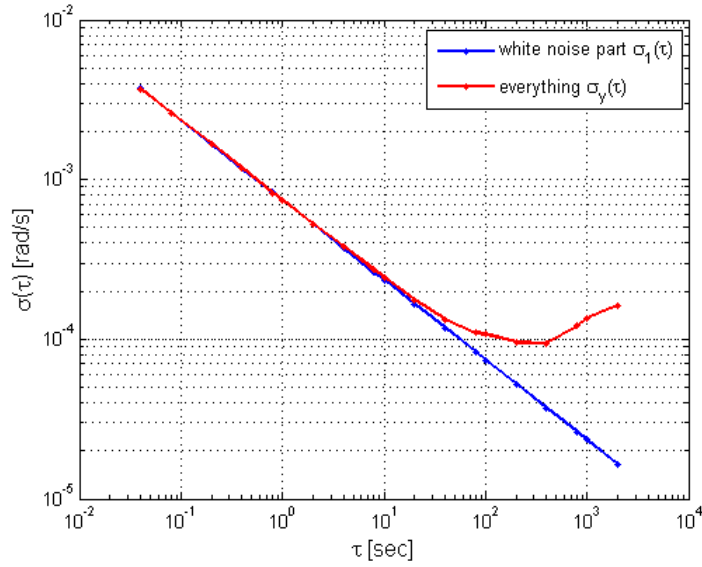


Figure 4.7: White noise part of the Allan deviation in comparison with the total.

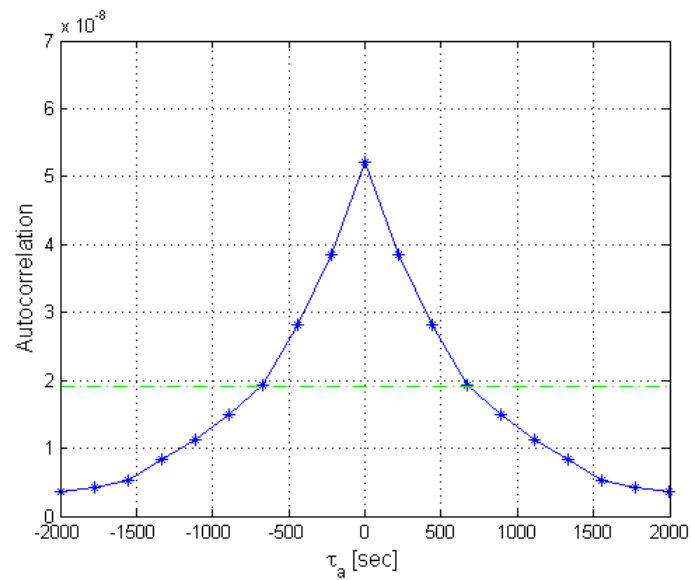


Figure 4.8: Auto-correlation function of the Allan deviation of exponentially correlated part of the noise (σ_2).

large, these parameters are given by approximately:

$$A_d = 1; \quad B_d = \Delta t_s = 0.04s$$

The bias instability coefficient B is calculated using the mean value when the slope is approximately zero, which is, in this case:

$$B = 4.411 \cdot 10^{-5} rad/s^2 \quad (4.14)$$

For the discrete time system, we have from equation (4.10):

$$\sigma_{bd} \approx B_d B \approx \Delta t_s B = 1.764 \cdot 10^{-6} rad/s \quad (4.15)$$

4.5.3 Final Model

Finally, the final model of the sensor noise for the angular rate in z axis from MicroStrain 3DM-GX3-25 can be obtained. Using equations 4.1 and 4.3, we can write:

$$\begin{cases} \tilde{\omega}_z = \omega_z + \beta + \eta_w & (a) \\ \beta(k+1) = \beta(k) + \eta_{bd} & (b) \end{cases} \quad (4.16)$$

where:

- $\tilde{\omega}_y$ is the measured angular rate in y axis;
- ω_y is the true angular rate in y axis;
- η_w is the Gaussian white-noise with deviation given by $3.781 \cdot 10^{-3} rad/s$.
- η_{bd} is the Gaussian white-noise with deviation given by $1.764 \cdot 10^{-6} rad/s$.

A signal was simulated using equation 4.16. Figure 4.9 illustrates the comparison between the Allan deviation of the simulated signal and the real one.

4.6 Results

The same procedure was done for all measurements of both sensors. In all cases, the approximation $A_d = 1$ and $B_d = \Delta t_s$ was used, since the correlation times were large enough. The results are summarized in table (4.1) for both the MicroStrain and Polulu instruments. The values of the white noise

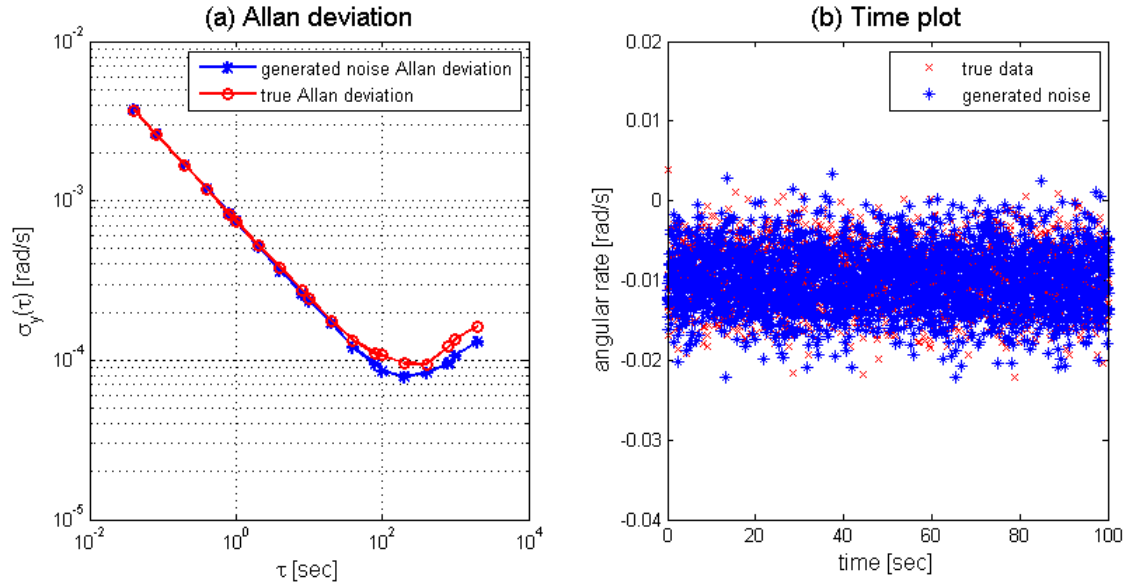


Figure 4.9: Real signal compared with the simulated signal.

Table 4.1: Noise coefficients for MicroStrain sensor

Sensor	Axis	MicroStrain		Polulu	
		N	B	N	B
Accelerometer	x	$0.1260 \cdot 10^{-3} g/\sqrt{\text{Hz}}$	$38.00 \cdot 10^{-6} g/s$	$1.028 \cdot 10^{-3} g/\sqrt{\text{Hz}}$	$0.1358 \cdot 10^{-3} g/s$
	y	$0.1316 \cdot 10^{-3} g/\sqrt{\text{Hz}}$	$23.09 \cdot 10^{-6} g/s$	$0.9975 \cdot 10^{-3} g/\sqrt{\text{Hz}}$	$0.1353 \cdot 10^{-3} g/s$
	z	$0.1541 \cdot 10^{-3} g/\sqrt{\text{Hz}}$	$62.71 \cdot 10^{-6} g/s$	$1.226 \cdot 10^{-3} g/\sqrt{\text{Hz}}$	$0.3815 \cdot 10^{-3} g/s$
Gyros	x	$0.7514 \cdot 10^{-3} \text{rad/s}/\sqrt{\text{Hz}}$	$32.67 \cdot 10^{-6} \text{rad/s}^2$	$0.5808 \cdot 10^{-3} \text{rad/s}/\sqrt{\text{Hz}}$	$0.1651 \cdot 10^{-3} \text{rad/s}^2$
	y	$0.7647 \cdot 10^{-3} \text{rad/s}/\sqrt{\text{Hz}}$	$26.03 \cdot 10^{-6} \text{rad/s}^2$	$0.5131 \cdot 10^{-3} \text{rad/s}/\sqrt{\text{Hz}}$	$16.54 \cdot 10^{-6} \text{rad/s}^2$
	z	$0.7416 \cdot 10^{-3} \text{rad/s}/\sqrt{\text{Hz}}$	$44.11 \cdot 10^{-6} \text{rad/s}^2$	$0.6241 \cdot 10^{-3} \text{rad/s}/\sqrt{\text{Hz}}$	$0.1721 \cdot 10^{-3} \text{rad/s}^2$
Magnetometer	x	$0.1520 \cdot 10^{-3} G/\sqrt{\text{Hz}}$	$46.57 \cdot 10^{-6} G/s$	$0.3649 \cdot 10^{-3} G/\sqrt{\text{Hz}}$	$0.1429 \cdot 10^{-3} G/s$
	y	$0.1082 \cdot 10^{-3} G/\sqrt{\text{Hz}}$	$66.68 \cdot 10^{-6} G/s$	$0.3778 \cdot 10^{-3} G/\sqrt{\text{Hz}}$	$0.1465 \cdot 10^{-3} G/s$
	z	$68.87 \cdot 10^{-6} G/\sqrt{\text{Hz}}$	$59.72 \cdot 10^{-6} G/s$	$0.3944 \cdot 10^{-3} G/\sqrt{\text{Hz}}$	$0.2540 \cdot 10^{-3} G/s$

coefficient N and bias instability coefficient B are listed. Note that the noise parameters are smaller in the MicroStrain sensor for almost every measurement. The only exceptions are the gyros white noise coefficients, which are almost the same for both sensors. However, the gyros drift coefficient is smaller in the MicroStrain sensor.

Additionally, the standard deviation of the white noise of the sensor η_w and of the white noise of the bias η_{bd} were calculated using the values of N and B in the previous table and the formulas (4.7) and (4.11). The standard deviations were calculated using using the sample time of 0.02s (or frequency of 50Hz), which is the sample time used in the tests and simulations in this thesis. The results are listed in the table 4.2.

Table 4.2: Noise coefficients for MicroStrain sensor

Sensor	Axis	MicroStrain		Polulu	
		σ_w	σ_{bd}	σ_w	σ_{bd}
Accelerometer	x	$0.8910 \cdot 10^{-3} \text{g}$	$0.7600 \cdot 10^{-6} \text{g}$	$7.266 \cdot 10^{-3} \text{g}$	$2.716 \cdot 10^{-6} \text{g}$
	y	$0.9306 \cdot 10^{-3} \text{g}$	$0.4619 \cdot 10^{-6} \text{g}$	$7.053 \cdot 10^{-3} \text{g}$	$2.706 \cdot 10^{-6} \text{g}$
	z	$1.090 \cdot 10^{-3} \text{g}$	$1.254 \cdot 10^{-6} \text{g}$	$8.667 \cdot 10^{-3} \text{g}$	$7.630 \cdot 10^{-6} \text{g}$
Gyros	x	$5.313 \cdot 10^{-3} \text{rad/s}$	$0.6534 \cdot 10^{-6} \text{rad/s}$	$4.107 \cdot 10^{-3} \text{rad/s}$	$3.301 \cdot 10^{-6} \text{rad/s}$
	y	$5.407 \cdot 10^{-3} \text{rad/s}$	$0.5206 \cdot 10^{-6} \text{rad/s}$	$3.628 \cdot 10^{-3} \text{rad/s}$	$0.3308 \cdot 10^{-6} \text{rad/s}$
	z	$5.244 \cdot 10^{-3} \text{rad/s}$	$0.8821 \cdot 10^{-6} \text{rad/s}$	$4.413 \cdot 10^{-3} \text{rad/s}$	$3.443 \cdot 10^{-6} \text{rad/s}$
Magnetometer	x	$1.075 \cdot 10^{-3} \text{G}$	$0.9314 \cdot 10^{-6} \text{G}$	$2.580 \cdot 10^{-3} \text{G}$	$2.857 \cdot 10^{-6} \text{G}$
	y	$0.7654 \cdot 10^{-3} \text{G}$	$1.334 \cdot 10^{-6} \text{G}$	$2.671 \cdot 10^{-3} \text{G}$	$2.929 \cdot 10^{-6} \text{G}$
	z	$0.4870 \cdot 10^{-3} \text{G}$	$1.194 \cdot 10^{-6} \text{G}$	$2.789 \cdot 10^{-3} \text{G}$	$5.081 \cdot 10^{-6} \text{G}$

Chapter 5

Kalman Filter Design

5.1 Introduction

Estimating the attitude from spacecraft on-board measurements has a long history. There are many common methods to describe the attitude such as Euler angles, quaternions, and Modified Rodrigues Parameters, as discussed in the survey [21] and presented in Chapter 2. Quaternions had been widely used because of their advantages, which include linear kinematic equations with respect to angular velocities and no singularities.

Considering the optimal algorithms to attitude estimation, there are two main approaches: the least-squares approach and the Kalman filtering approach [3]. The first approach was originally introduced in the so-called Wahba's problem, which is a constrained least-squares minimization problem for finding the attitude matrix. Later, the Wahba's problem was formulated and solved in terms of the attitude quaternion, which became known in the literature as the q-method [3]. The Kalman filtering approach, on the other hand, yields sequential attitude parameters estimates that are minimum-variance. One of the main advantages of using the Kalman filter is that it is recursive, eliminating the necessity for storing large amounts of data, making it simpler for real time applications. Another advantage is that time varying coefficients are permitted in the model. Therefore, the Kalman filter is normally preferred in attitude estimation problems.

Nonetheless, it is important to remember that the quaternion components are non-minimal. There are four components and a constraint that the quaternion must have unit norm. The quaternion normalization constraint produces a singularity in the Kalman filter covariance matrix [5]. There are many solutions to this problem, as shown in [3, 6], such as the multiplicative or the additive approach using

quaternions errors.

Here, this problem was solved in 2 ways:

- First approach: the quaternion normalization is included in the state equation, eliminating the need of a normalization step and assuring non-singularity in the covariance matrix. This methodology is described in section 5.5. The advantages of this approach over the usual Kalman filter mechanization for spacecraft attitude is that it deals with the whole attitude rather than with incremental corrections.
- Second approach: use a three-dimensional parametrization known as the modified Rodrigues parameters (MRP) [5], presented in Chapter 2. It is known that all three-dimensional parametrization have singularities, but the MRP allow rotation up to 360 degrees, making it a convenient attitude representation for attitude feedback control.

5.2 Attitude Kinematics

5.2.1 Rigid Body Dynamics

The rigid body angular motion obeys the vector differential equation [15]:

$$\dot{q}(t) = \frac{1}{2} q(t) \otimes \omega(t) \quad (5.1)$$

which is given by a simple quaternion product (to more details about the operations involved in quaternion multiplication, see 2.4). The symbol $\omega(t)$ represents the angular velocity in the body frame.

The rigid body angular motion can also be described in terms of MRP, which is given by [5]:

$$\dot{p}(t) = \frac{1}{2} \left(\frac{1}{2} (1 - p^T(t)p(t)) I_{3 \times 3} + [p(t) \times] + p(t)p^T(t) \right) \omega(t). \quad (5.2)$$

The discrete time model corresponding to equations (5.1) and (5.2) are respectively:

$$q_{k+1} = q_k + \frac{\Delta t_s}{2} q_k \otimes \omega_k, \quad (5.3)$$

$$p_{k+1} = p_k + \frac{\Delta t_s}{2} \left(\frac{1}{2} (1 - p_k^T p_k) I_{3 \times 3} + [p_k \times] + p_k p_k^T \right) \omega_k, \quad (5.4)$$

assuming a constant sample rate Δt_s and assuming the angular velocity is constant over the sample period. Exact discretization is very computational demanding due to the heavy matrix exponential op-

erations involved. The discrete models showed in equations (5.3) and (5.4) are approximations using a first order Taylor expansion $e^{A\Delta t} \approx I + A\Delta t$. This approximation is considered sufficiently accurate for small time steps and is well suited for the real-time application in the satellite simulator, where the filter is going to be implemented.

5.2.2 Rigid Body Orientation

The orientation of a rigid body in space is determined when the orientation of a coordinate frame attached to the body is specified with respect to the Earth inertial frame. The three-axis accelerometer and magnetometer are fixed to the body frame, hence they measure components of the gravity and of the earth magnetic field in the body frame. As the gravity and magnetic field vectors are known and constant for a limited geographic area, one can expect that there exists a quaternion relating the measurements (values in body frame) to the real magnetic and gravity fields (values in Earth inertial frame).

The transformation between the representations can be accomplished by using an attitude matrix obtained from the quaternions or MRP, presented in equation (2.9). The transformation between the representations, from inertial I to body B frame, of the 3×1 column-vector with accelerations (a) and of the 3×1 column-vector with magnetic field measurements (h) are:

$$\begin{cases} a^B = R_I^B a^I \\ h^B = R_I^B h^I \end{cases} \quad (5.5)$$

where R_I^B is the attitude matrix, which can be defined in terms of quaternions or MRP, as presented in equations (2.10) and (2.14). They were repeated here for completeness.

$$R_I^B(q) = \begin{bmatrix} 1 - 2(q_2^2 + q_3^2) & 2(q_1 q_2 + q_0 q_3) & 2(q_1 q_3 - q_0 q_2) \\ 2(q_1 q_2 - q_0 q_3) & 1 - 2(q_1^2 + q_3^2) & 2(q_2 q_3 + q_0 q_1) \\ 2(q_1 q_3 + q_0 q_2) & 2(q_2 q_3 - q_0 q_1) & 1 - 2(q_1^2 + q_2^2) \end{bmatrix} \quad (5.6)$$

$$R_I^B(p) = I_{3 \times 3} - \frac{4(1 - p^T p)}{(1 + p^T p)^2} [p \times] + \frac{8}{(1 + p^T p)^2} [p \times]^2 \quad (5.7)$$

5.3 Pre-filter step

Before using the sensor measurements to estimate the attitude of the body, they must be corrected in order to eliminate the determinist part of the error, such as scale factors, fixed bias, and misalignment (see

chapter 3). This correction is named “the pre-filter step”. The pre-filter simply consists in utilizing the raw measurements from the sensors and the calibration parameters previously calculated to produce as a result the measured angular rate (ω), acceleration (a), and magnetic field (h) in the body frame coordinates. Equation (5.8) demonstrates the operations of the pre-filter step for the angular rates. The 3×1 vector v_{ω}^M is formed with raw values read from the angular rate sensor and $\tilde{\omega}$ is the 3×1 angular rate vector measurement corrected for deterministic errors.

$$\begin{bmatrix} \tilde{\omega}_x \\ \tilde{\omega}_y \\ \tilde{\omega}_z \end{bmatrix} = \begin{bmatrix} c_1 & c_2 & c_3 \\ c_5 & c_6 & c_7 \\ c_9 & c_{10} & c_{11} \end{bmatrix} \begin{bmatrix} v_{\omega x}^M \\ v_{\omega y}^M \\ v_{\omega z}^M \end{bmatrix} + \begin{bmatrix} c_4 \\ c_8 \\ c_{12} \end{bmatrix}. \quad (5.8)$$

The same procedure is applied for the accelerations and magnetic fields. Except in the case of the magnetometer of the MicroStrain IMU. The calibration parameters were written on its non-volatile memory and the pre-filter step is already performed internally in the sensor in this case.

5.4 Sensor Model

After the deterministic part of the error is corrected, the stochastic part of the sensor error is modeled using equation (4.1). The equations for the vectors angular rate, acceleration, and magnetic field are expressed as:

$$\begin{cases} \tilde{\omega} = \omega + \beta_{\omega} + \eta_{\omega} \\ \tilde{a} = R_I^B a^I + \beta_a + \eta_a \\ \tilde{h} = R_I^B h^I + \beta_h + \eta_h \end{cases} \quad (5.9)$$

where:

- $\tilde{\omega}$, \tilde{a} , and \tilde{h} are the measured angular rates, accelerations and magnetic fields vectors, with dimension (3×1) . They were already corrected for deterministic errors in the pre-filter step;
- ω is the true angular rate vector, with dimension (3×1) ;
- a^I is the gravity vector in the inertial frame, given by $[0 \ 0 \ -1]^T g$ for the region of Logan, Utah.
- h^I is the magnetic field vector in the inertial frame, given by $[0.21 \ 0 \ 0.48]^T$ Gauss for the region of Logan, Utah.

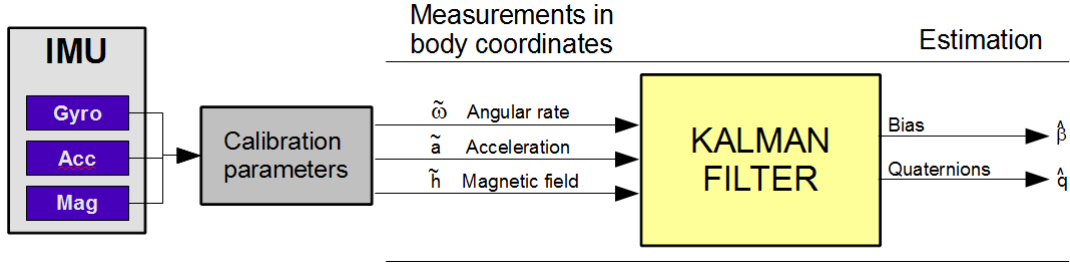


Figure 5.1: Block diagram of the first approach of the Kalman filter.

- β_ω , β_a , and β_h are the drift-rate bias vector of the gyroscope, accelerometer and magnetometer, with dimension (3×1) ;
- η_ω , η_a , and η_h are the Gaussian white-noise vector of the measurements, with dimension (3×1) .
The mean is zero and its standard deviations are given in table 4.2.

The drift-rate bias was modeled as a first order Gauss-Markov process, as showed in equations (4.2) for continuous time and (4.3) for discrete time. The discrete time formula can be simplified as:

$$\begin{cases} [\beta_\omega]_{k+1} = [\beta_\omega]_k + \Delta t_s \eta_{b\omega} \\ [\beta_a]_{k+1} = [\beta_a]_k + \Delta t_s \eta_{ba} \\ [\beta_h]_{k+1} = [\beta_h]_k + \Delta t_s \eta_{bh} \end{cases} \quad (5.10)$$

where $\eta_{b\omega}$, η_{ba} , and η_{bh} are the Gaussian white-noise vector of the bias, with dimension (3×1) . The mean is zero and its standard deviations are given in table 4.2 as well.

5.5 First Approach

This approach was based on the work presented on the papers [16, 17, 28]. The block diagram in figure 5.1 displays a simple scheme of the first approach of the filter. This section aims to describe how the Kalman filter produces quaternions and bias estimates from the IMU measurements.

5.5.1 The State Vector

The state vector is defined here to be composed with variables that are important for the attitude determination which cannot be measured. As a consequence, they need to be estimated by the Kalman filter. The chosen components for the state vector x are the four quaternion components, and the drift-rate bias vectors of the rate sensors, accelerometers and magnetometers, as expressed in equation (5.11).

$$x = [q_0 \quad q_1 \quad q_2 \quad q_3 \quad \beta_{\omega x} \quad \beta_{\omega y} \quad \beta_{\omega z} \quad \beta_{ax} \quad \beta_{ay} \quad \beta_{az} \quad \beta_{hx} \quad \beta_{hy} \quad \beta_{hz}]^T. \quad (5.11)$$

5.5.2 State Equations

The states are described by rigid body dynamic and bias drift equations, which are given by equations (5.12) and (5.10). It is important to remember that a quaternion must have unit-norm. The unit-norm property of the a posteriori quaternion must be preserved by dividing it by its Euclidean norm. Since the sample time is very small, in one iteration the values of q_{k+1} and q_k and almost the same. Therefore, dividing the expression in parenthesis in equation (5.12) by $|q_k|$ it is enough to ensure a unit quaternion.

$$q_{k+1} = (q_k + \frac{\Delta t_s}{2} q_k \otimes \omega_k) \frac{1}{|q_k|}. \quad (5.12)$$

The variable ω_k represents the true angular velocity vector with dimension 3×1 in the time k and it is given by $\omega_k = \tilde{\omega}_k - \beta_{\omega k} - \eta_{\omega k}$.

The expansion of equation (5.12) yields then

$$\begin{bmatrix} q_0 \\ q_1 \\ q_2 \\ q_3 \end{bmatrix}_{k+1} = \frac{1}{\sqrt{q_0^2 + q_1^2 + q_2^2 + q_3^2}} \left(\begin{bmatrix} q_0 \\ q_1 \\ q_2 \\ q_3 \end{bmatrix}_k + \frac{\Delta t_s}{2} \begin{bmatrix} -q_1 \omega_x - q_2 \omega_y - q_3 \omega_z \\ q_0 \omega_x - q_3 \omega_y + q_2 \omega_z \\ q_3 \omega_x + q_0 \omega_y - q_1 \omega_z \\ q_1 \omega_y - q_2 \omega_x + q_0 \omega_z \end{bmatrix}_k \right). \quad (5.13)$$

From equations (5.13) and (5.10), the state model equations are:

$$\begin{cases} q_{k+1} = f_1(q_k, \beta_{\omega k}, \tilde{\omega}_k, \eta_{\omega}) \\ \beta_{k+1} = f_2(\beta_k, \eta_b) \end{cases} \quad (5.14)$$

with $\eta_b = [\eta_{b\omega} \quad \eta_{ba} \quad \eta_{bh}]^T$ being a 9×1 vector with the Gaussian white-noise of the bias of all sensors.

The extended Kalman filter linearizes these equations using the partial derivatives (see equations (2.27)) in order to obtain a state-model equation given by

$$x_{k+1} = F_k x_k + W_k w_k, \quad (5.15)$$

with the states as in equation (5.11), $w = [\eta_\omega \quad \eta_b]^T$, and $E[w_k w_k^T] = Q$. The process noise w has a fixed variance, calculated in Chapter 4, using the Allan variance method. Consequently, matrix Q is diagonal matrix yields

$$Q = \text{diag}(\sigma_{w,\omega_x}^2, \sigma_{w,\omega_y}^2, \sigma_{w,\omega_z}^2, \sigma_{bd,\omega_x}^2, \sigma_{bd,\omega_y}^2, \sigma_{bd,\omega_z}^2, \sigma_{bd,a_x}^2, \sigma_{bd,a_y}^2, \sigma_{bd,a_z}^2, \sigma_{bd,h_x}^2, \sigma_{bd,h_y}^2, \sigma_{bd,h_z}^2). \quad (5.16)$$

The matrices F_k and W_k are listed in Appendix A.

5.5.3 The Outputs

The outputs are values that must be estimated and compared to measurements coming from the sensors. In this case, it is possible to estimate the gravity vector and the local magnetic field vector in the body frame using the orientation parameters estimated by the filter (quaternions). In other words, the known values of gravity and earth magnetic field in Earth coordinates are converted into body coordinates using the quaternions. Therefore, the output vector can be expressed by

$$z = [\tilde{a}_x \quad \tilde{a}_y \quad \tilde{a}_z \quad \tilde{h}_x \quad \tilde{h}_y \quad \tilde{h}_z]^T. \quad (5.17)$$

The output equations must also include the bias drifts and the measurement noise. The complete equations are

$$\begin{cases} \tilde{a} &= R_I^B a^I + \beta_a + \eta_a \\ \tilde{h} &= R_I^B h^I + \beta_h + \eta_h \end{cases}. \quad (5.18)$$

In order to obtain the linearized version, the Jacobian matrix H_k of partial derivatives relating the states to the measurements and the Jacobian matrix V_k of partial derivatives relating the noises to the measurements must be calculated. The result is a state-space measurement equation

$$z_k = H_k x_k + V_k \varepsilon_k, \quad (5.19)$$

with $\varepsilon = [\eta_a \quad \eta_h]^T$, and $E[\varepsilon_k \varepsilon_k^T] = R$. The measurement noise ε has a fixed standard deviation, exposed in table 4.2. Hence,

$$R = \text{diag}(\sigma_{w,a_x}^2, \sigma_{w,a_y}^2, \sigma_{w,a_z}^2, \sigma_{w,h_x}^2, \sigma_{w,h_y}^2, \sigma_{w,h_z}^2). \quad (5.20)$$

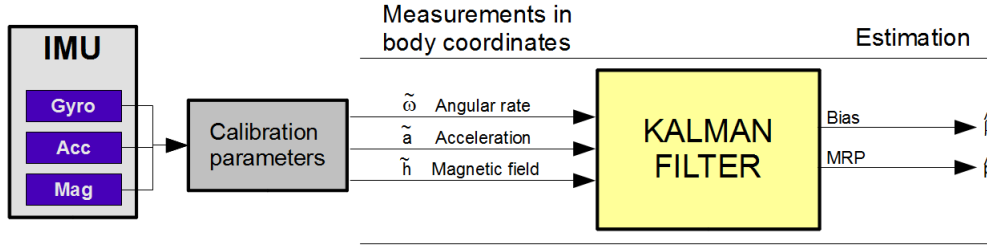


Figure 5.2: Block diagram of the second approach of the Kalman filter.

The V_k matrix is simply the identity matrix with dimension 6 and H_k is in Appendix A.

$$\begin{cases} \hat{a}_k = R_I^B(\hat{q}_k) a^I + \hat{\beta}_{ak} \\ \hat{h}_k = R_I^B(\hat{q}_k) h^I + \hat{\beta}_{hk} \end{cases} \quad (5.21)$$

The equations (5.21) are the EKF measurement equations, which can be written as

$$\hat{z}_k = h(\hat{x}_k, 0).$$

Finally, they are compared to the measured values in body coordinates coming from the sensors (\tilde{a} and \tilde{h}).

5.6 Second Approach

This second approach was based on the paper of Crassidis and others [5]. It has the same principle as the first approach with the only difference that modified Rodrigues parameters are used instead of quaternions.

5.6.1 The State Vector

The components for the state vector x are the three MRP components, instead of the four quaternions, and the drift-rate bias vectors of the rate sensors, accelerometers and magnetometers. Hence, this approach has 12 states instead of 13.

$$x = [p_1 \ p_2 \ p_3 \ \beta_{\omega x} \ \beta_{\omega y} \ \beta_{\omega z} \ \beta_{ax} \ \beta_{ay} \ \beta_{az} \ \beta_{hx} \ \beta_{hy} \ \beta_{hz}]^T. \quad (5.22)$$

5.6.2 State Equations

The states are described by rigid body dynamic and bias drift equations which are given by equations (5.4) and (5.10) respectively. Those equations can be rewritten in the form:

$$\begin{cases} p_{k+1} = f_1(p_k, \beta_{\omega k}, \tilde{\omega}_k, \eta_\omega) \\ \beta_{k+1} = f_2(\beta_k, \eta_b) \end{cases}, \quad (5.23)$$

or in the linearized form:

$$x_{k+1} = F_k x_k + W_k w_k, \quad (5.24)$$

with the states as in equation (5.22), $w = [\eta_\omega \quad \eta_b]^T$, and $E[w_k w_k^T] = Q$. The process covariance matrix Q is the same as in the first approach, indicated in equation (5.16). The other matrices can be seen in Appendix A.

5.6.3 The Outputs

The outputs are exactly the same in the first approach, as in equation (5.17). The only difference is that the rotation matrix is obtained in terms of the modified Rodrigues parameters instead of quaternions.

$$\begin{cases} \hat{a}_k = R_I^B(\hat{p}_k) a^I + \hat{\beta}_{ak} \\ \hat{h}_k = R_I^B(\hat{p}_k) h^I + \hat{\beta}_{hk} \end{cases}. \quad (5.25)$$

The Jacobian matrix H_k relating the states x_k to the measurements z_k can be seen in Appendix A.

5.7 Extended Kalman Filter Loop

5.7.1 Initialization

To start the Kalman filter loop, one must obtain the initial estimates of the states (\hat{x}_0^-) and of the covariance matrix (P_0^-). The states can be divided in two parts: attitude parametrization vector (quaternions or MRP) and bias vector. The bias vector initial estimate is zero ($\hat{\beta}_0^- = 0_{9 \times 1}$), which is a good first estimate of IMU bias. However, to obtain the initial quaternions (first approach) or MRP (second approach), a more elaborated estimation is conducted. The orientation estimates are obtained in first in terms of Euler angles (roll, pitch and yaw) and then converted into quaternions (first approach) or MRP (second

approach).

At the beginning of the tests, the initial orientation of the aluminum “cube” with the IMUs is known to be with z-axis of the sensors pointing up. Hence, the roll and pitch Euler angles are approximately zero. The initial yaw angle can be estimated using the magnetic field measurements. Thus,

$$\begin{cases} \phi = 0; \\ \theta = 0; \\ \psi = \tan 2^{-1}(-h_y, h_x), \end{cases}$$

where ϕ is the roll angle, θ is the pitch and ψ is the yaw angle. The operation $\tan 2^{-1}$ is the arc-tangent function with two arguments. The purpose of using two arguments instead of one, is to gather information of the signs of the inputs in order to return the appropriate quadrant of the computed angle, which is not possible for the single-argument arc-tangent function.

The Euler angles can be converted to quaternions by using the following trigonometric identities:

$$\begin{bmatrix} q_0 \\ q_1 \\ q_2 \\ q_3 \end{bmatrix} = \begin{bmatrix} \cos(\psi/2) \cos(\theta/2) \cos(\phi/2) + \sin(\psi/2) \sin(\theta/2) \sin(\phi/2) \\ \cos(\psi/2) \cos(\theta/2) \sin(\phi/2) - \sin(\psi/2) \sin(\theta/2) \cos(\phi/2) \\ \cos(\psi/2) \sin(\theta/2) \cos(\phi/2) + \sin(\psi/2) \cos(\theta/2) \sin(\phi/2) \\ \sin(\psi/2) \cos(\theta/2) \cos(\phi/2) - \cos(\psi/2) \sin(\theta/2) \sin(\phi/2) \end{bmatrix}. \quad (5.26)$$

In the case of the second approach, the MRP are obtained from the quaternions using equation (2.12).

From there, it is possible to calculate the initial matrices F_0 , W_0 and H_0 .

The initialization of the covariance matrix was simpler. It was initialized as

$$P_0^- = I_{n \times n},$$

with $n = 13$ for the first approach and $n = 12$ for the second approach.

To finalize the initialization step, the process covariance matrix Q and the measurement covariance matrix R are defined as in equations (5.16) and (5.20). They are constant matrices which don't change throughout the Kalman loop.

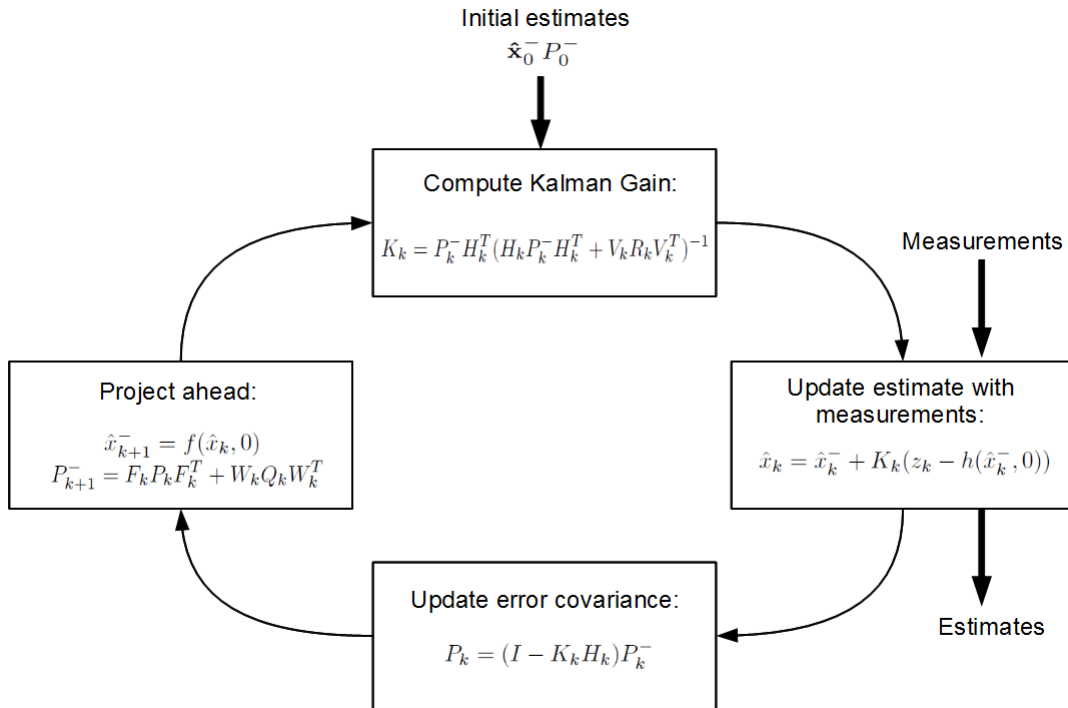


Figure 5.3: EKF loop. Based on [2].

5.7.2 The Loop

After the initialization process, the Kalman gain is calculated. Next, the states and the covariance matrix are updated. Finally, the states and the covariance matrix are propagated ahead to the next iteration. The diagram in figure 5.3 summarizes the operations involved in the extended Kalman filter loop. Note that the Kalman filter uses the measurements as inputs and produces estimates of the states as outputs.

Chapter 6

Implementation and Testing

This chapter is divided into two parts. The first part looks into the simulations and introduces the calculations of the Euler angles and the angle of rotation error, used throughout this section. It also compares the results of the quaternion and MRP approaches. The second part looks into the evaluation of the performance of the extended Kalman filter tested with the air bearing table and the IMUs.

6.1 Simulation Environment

Both Kalman filter approaches are tested in a simulation environment to investigate the performance and the accuracy of the algorithm. The measurements of acceleration, angular rates and magnetic fields are simulated instead of read from the sensors. In this way, the truth attitude can be compared with the estimated attitude in order to evaluate the performance of the algorithm.

6.1.1 Generation of the Simulated Measurements

The measurements of the IMUs were simulated using Matlab in a way to be as close as possible to the real values. Hence, the sample time was chosen to match the real one that was used in the tests ($\Delta t_s = 0.02\text{s}$); and the standard deviation of the errors are the same as the standard deviation of the real sensors, listed in table 4.2.

The following procedure was conducted to generate the simulated IMU measurements:

1. The angular rate ω was chosen to be a constant value of 10 deg/s about the z -axis and null in the other axis. This simulates the rotation of the instruments in the air bearing table with the z -axis facing up.

2. From the value of ω , the truth quaternions were obtained using the rigid body dynamics, in equation (5.1).
3. From the quaternions, the true accelerations and magnetic fields were generated using the attitude matrix R_I^B , from equation (5.5).
4. Then, the accelerations, magnetic fields and angular rates truth values were corrupted with white noise and bias random walk accordingly with equation (5.9).

The results are displayed in figure 6.1. It shows the simulated measurements of angular rates, magnetic fields, and accelerations in all three axis. The truth value is shown in red, while the measurements with white noise and walking bias are shown in blue with the MicroStrain's noise parameters and in green with the Pololu's noise parameters. This simulated measurements are going to be used in the Kalman filter algorithm to estimate the attitude using both approaches: quaternions and MRP.

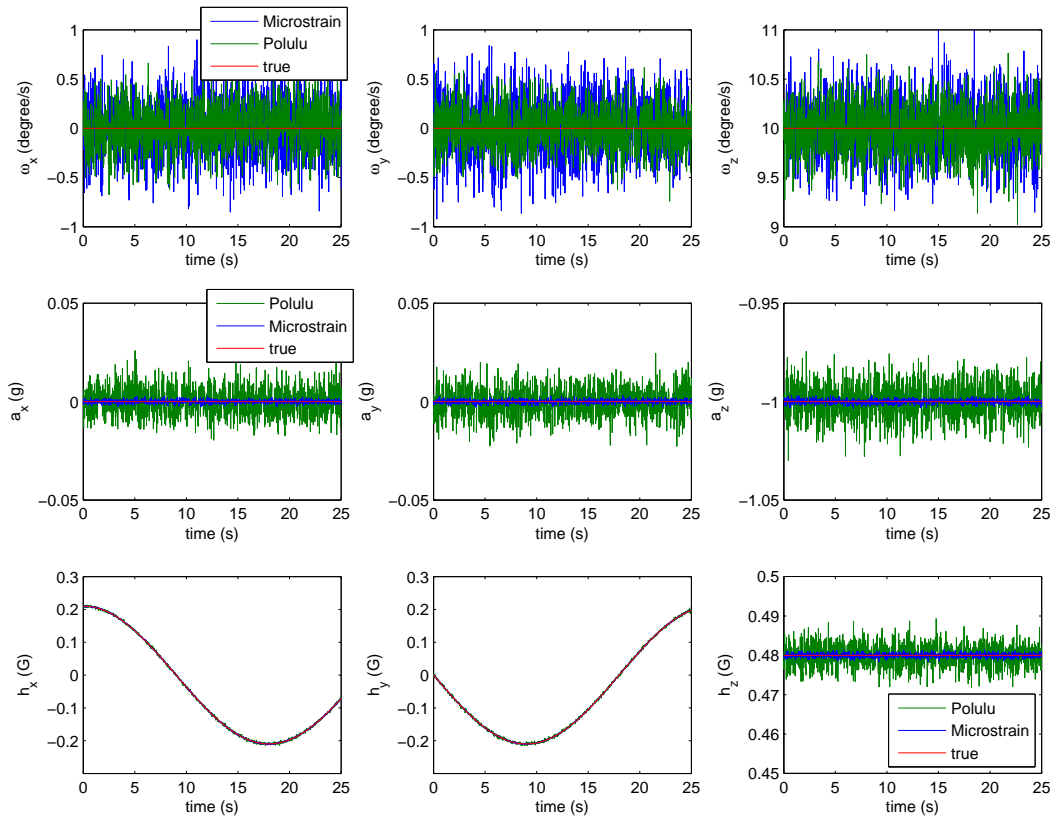


Figure 6.1: Simulated measurements of MicroStrain in blue and Pololu in green. The truth values are in red.

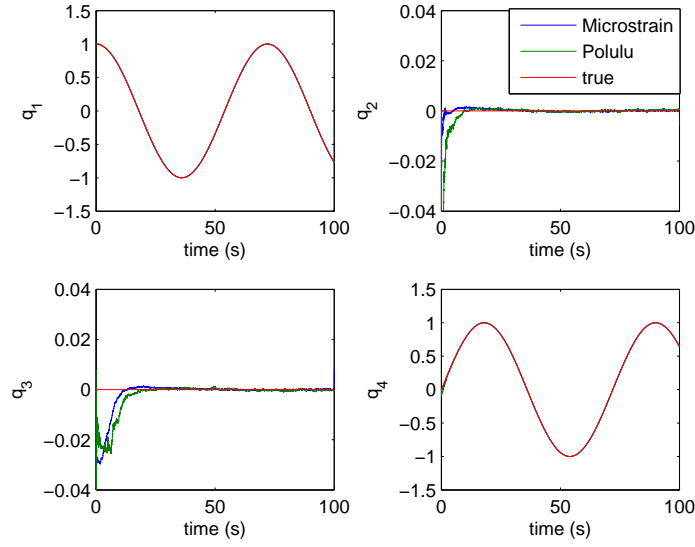


Figure 6.2: Quaternions of the simulation.

6.1.2 Kalman Filter Estimation

Using the simulated measurements as inputs, the Kalman filter algorithm gives the estimated quaternions or MRP, and the estimated biases. In order to be able to visualize the orientation of the body, the quaternions or the MRP are converted to Euler angles: roll (ϕ), pitch (θ) and yaw (ψ) angles. This conversion is done using the attitude matrix R_I^B , which can be obtained from equation (2.10) for the quaternion or equation (2.14) for the MRP. The Euler angles are got from the following relations:

$$\begin{cases} \phi = \tan^{-1}(R_I^B(2,3), R_I^B(3,3)); \\ \theta = \sin^{-1}(-R_I^B(1,3)); \\ \psi = \tan^{-1}(R_I^B(1,2), R_I^B(1,1)). \end{cases} \quad (6.1)$$

These relations give yaw between $-\pi$ rad (or -180°) and π rad (or 180°).

6.1.2.1 Quaternion Approach

In order to measure the performance of the filter, the quaternion error is calculated. It is defined as [5]:

$$\delta q = q \otimes \hat{q}^{-1}, \quad (6.2)$$

where q is the true quaternion and \hat{q} is the estimated quaternion. From the quaternion error, it is possible to obtain the error in the angle of rotation θ_r , which is given by:

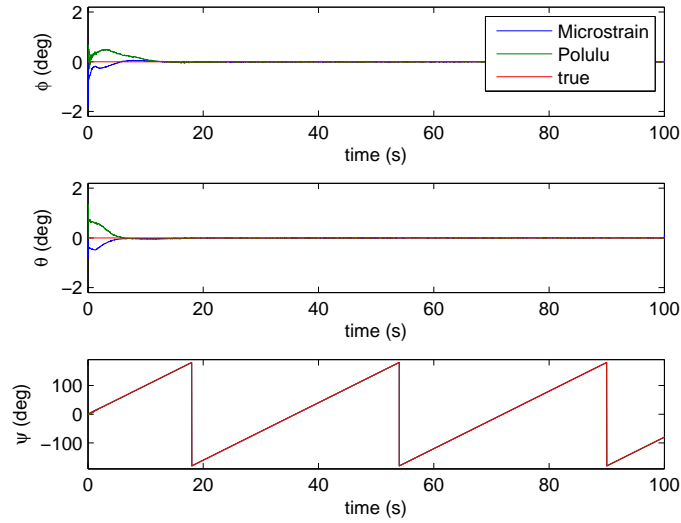


Figure 6.3: Euler angles of the first approach simulation.

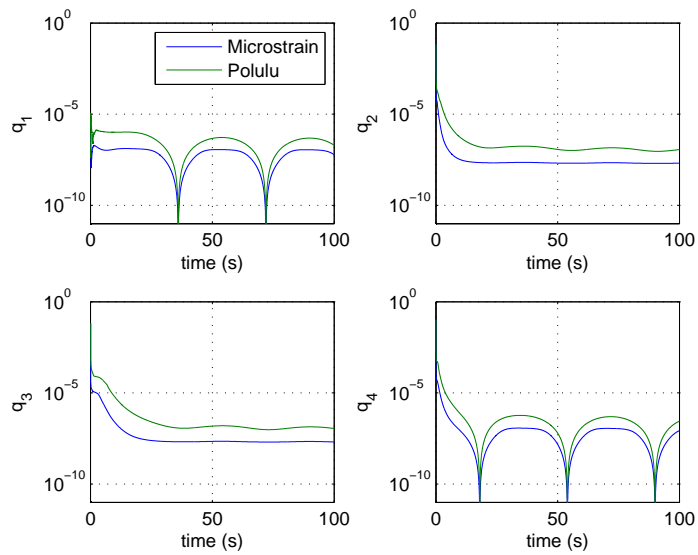


Figure 6.4: Covariances of the first approach simulation.

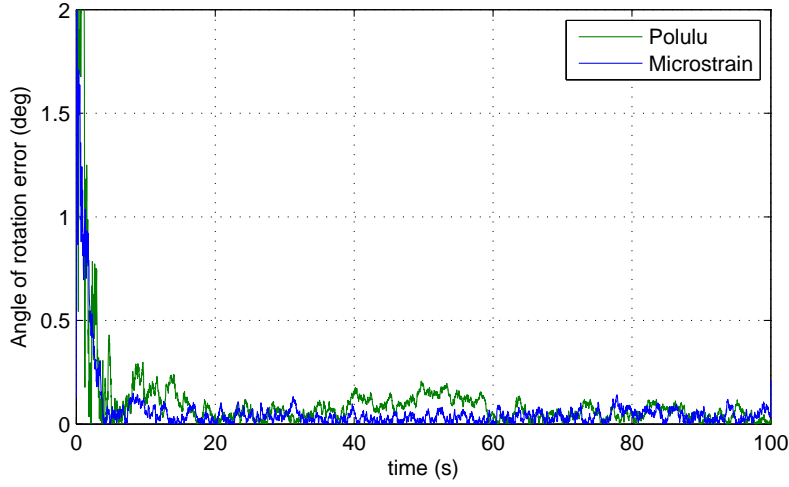


Figure 6.5: Angle of rotation errors of the quaternion simulation.

$$\delta\theta_r = 2 \cdot \cos^{-1}(\delta q_0). \quad (6.3)$$

This relation is derived from equation (2.5).

A plot comparing the absolute value of the error in the angle of rotation for the MicroStrain and Pololu simulated measurements are shown in figure (6.9). In the first seconds, the error is larger due to the time needed for the filter to converge. It can be seen that the error is smaller for the MicroStrain sensors, due to the smaller noise parameters. A comparison of the mean values of the angle of rotation errors gives a better idea of how much smaller the error for the Microstrain sensor is :

- $\delta\bar{\theta}_r = 0.065^\circ$ for the MicroStrain. If eliminating the first 5 seconds, the mean is 0.039° .
- $\delta\bar{\theta}_r = 0.108^\circ$ for the Pololu. If eliminating the first 5 seconds, the mean is 0.072° .

The error of the estimated attitude using the measurements of the MicroStrain is approximately half of the error of the Pololu.

6.1.2.2 Modified Rodrigues Parameters Approach

The MRP have a singularity in the 360° . For that reason, the simulation was performed during 32 seconds only, conferring a rotation of 320° and avoiding the singularity. The results of the simulations are exposed on the plots 6.6, 6.7 and 6.8. In all of them, the true MRP is shown in red while the estimated MRP are shown in blue and green for MicroStrain and Pololu respectively. Figure 6.6 presents the MRP while the roll, pitch and yaw attitude angles are shown in figure 6.7. Plots of the attitude covariance are

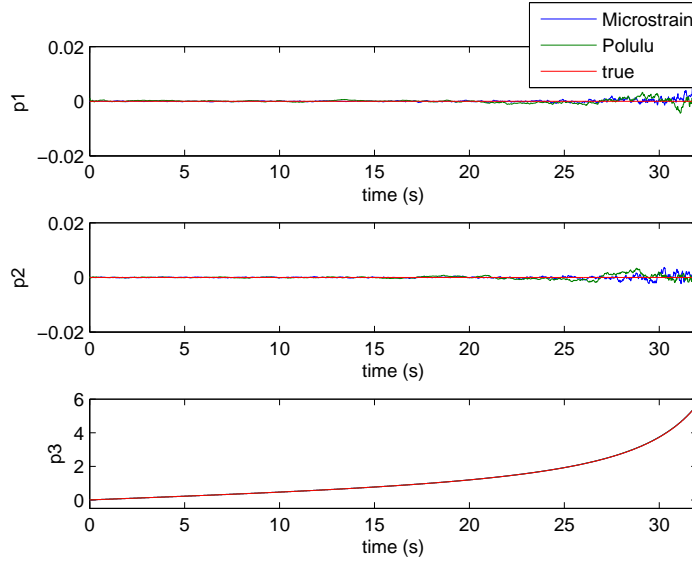


Figure 6.6: Modified Rodrigues Parameters.

shown in figure 6.8. It can be noticed that the MRP covariance increases as the rotation approaches 360° (getting closer to the singularity).

In order to measure the performance of the filter, the MRP error is calculated. It is defined as [5]:

$$\delta p = p \otimes \hat{p}^{-1}, \quad (6.4)$$

where p is the true quaternion and \hat{p} is the estimated quaternion. The composition rule for the MRP leads to the following expression (considering small δp):

$$\delta p = [(1 - |\hat{p}|^2)I_{3 \times 3} + 2[\hat{p} \times] + 2\hat{p}\hat{p}^T]^{-1}(p - \hat{p}). \quad (6.5)$$

More details can be obtained in [5]. As the parameter p_3 is bigger than the other two in this simulation (see figure 6.6), it is possible to use the approximation that the majority of the error is due to p_3 . Therefore, the error in the angle of rotation θ_r can be obtained from equation (2.11) and it is given by:

$$\delta \theta_r = 4 \cdot \tan^{-1}(\delta p_3). \quad (6.6)$$

A plot comparing the error in the angle of rotation using the measurements of the MicroStrain and Pololu sensors are shown in figure (6.9). It is clear that, in the first seconds, the error in the estimation is smaller for the MicroStrain sensors, however it approximates with the Pololu's error towards the end. One can compare the mean value of the errors:

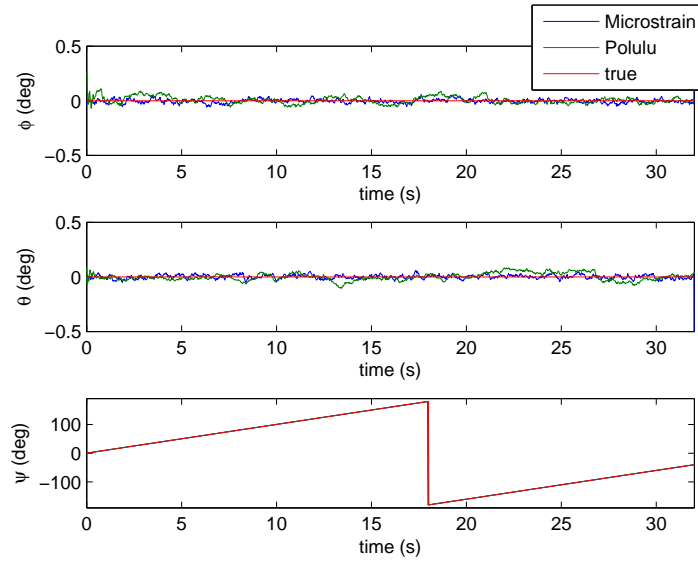


Figure 6.7: Euler angles of the second approach simulation.

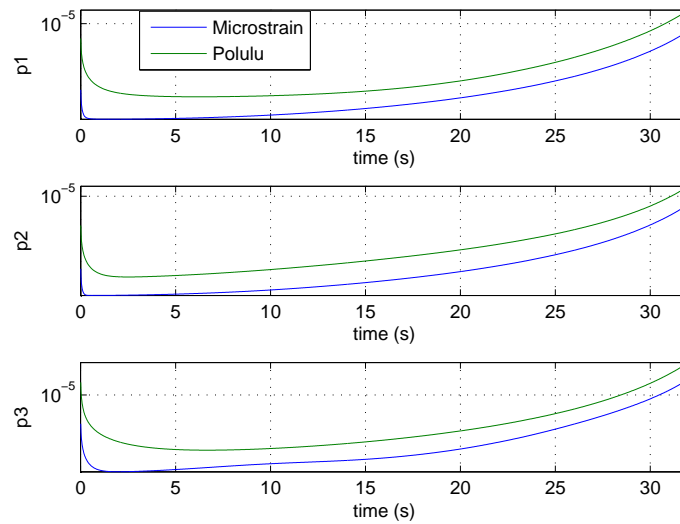


Figure 6.8: Covariances of the second approach simulation.

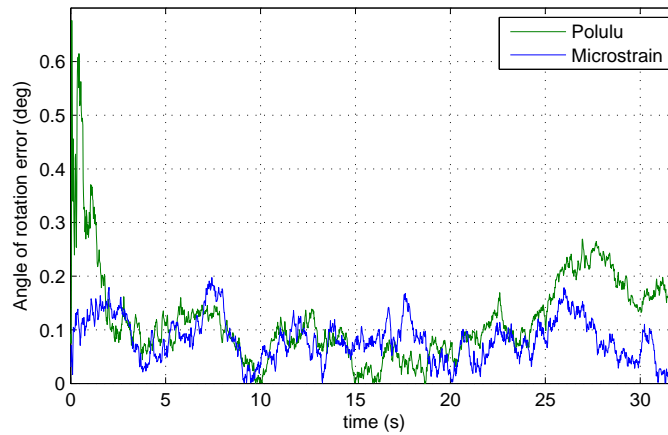


Figure 6.9: Angle of rotation errors of the MRP simulation.

- 0.082° for the MicroStrain. If eliminating the first 10 seconds, the mean is 0.079° .
- 0.120° for the Pololu. If eliminating the first 10 seconds, the mean is 0.108° .

The results show again that the error is smaller for the MicroStrain sensors, since it has smaller noise parameters.

6.1.3 Conclusions about the Simulations

Both extended Kalman filters developed in this thesis proved to be able to accurately estimate the attitude in the simulated conditions. After the first seconds, both Kalman filters converged to an accurate estimation of attitude.

However, the approach using MRP achieved a worse degree of accuracy compared to the approach with quaternions. This differences can be explained by the different ways to calculate the angle of rotation error. Several approximations were used in the MRP case, which could result in slightly different results, as observed.

One drawback of the MRP is the existing singularity for 360 degrees of rotation. The simulation satellite is predicted to rotate freely in more than 360 degrees. Therefore, the quaternion approach was chosen to be implemented in the real time system of the satellite simulator, as it has no singularities. Because of this, the quaternion approach is tested with the IMUs and the air bearing table and the results are in the next section.

It is important to mention that solutions to this singularity problem in the MRP Kalman filter have been proposed, as allowing for a discrete jump to the origin when the rotation approaches the singularity [5].

6.2 Test with the Air-Bearing Table

The aim of the test is to verify if the simulation results can be replicated with the experimental setup.

The aluminum “cube” with sensor and BB was fixed on the air bearing table to conduct the tests. The sensors were mounted on the table with the z-axis of the instruments facing up. The air bearing table was placed on the level platform so that all movement is around the z-axis only. The whole assembly is illustrated in figure 6.10. With this configuration, the rotation is about only one axis, permitting the orientation estimation from the EKF to be compared with the high precision encoder measurements.

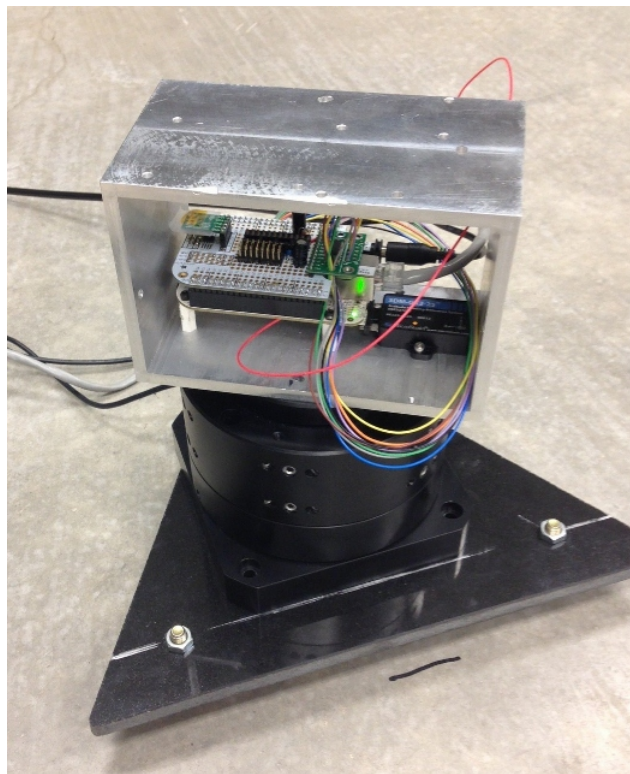


Figure 6.10: Level planar air bearing with mounted sensors and BB.

The test was performed in the following manner. The x-axis of the instruments were pointed facing the north direction as the initial position. The table was manually turned in one direction and then turned in the opposite direction until the x-axis was approximately pointing North direction again. Figure 6.11 presents the measured angular rates, accelerations and magnetic fields from both IMUs, with MicroStrain in blue and Pololu in green. This measurements were already treated in the pre-filter phase, which means they were already multiplied by the calibration matrices to get rid of deterministic errors, as discussed in chapter 5. In the plot of the angular rates of the z-axis (ω_z), the true value is also plotted, in red. The true angular rate was obtained by deriving the angular position given by the encoder.

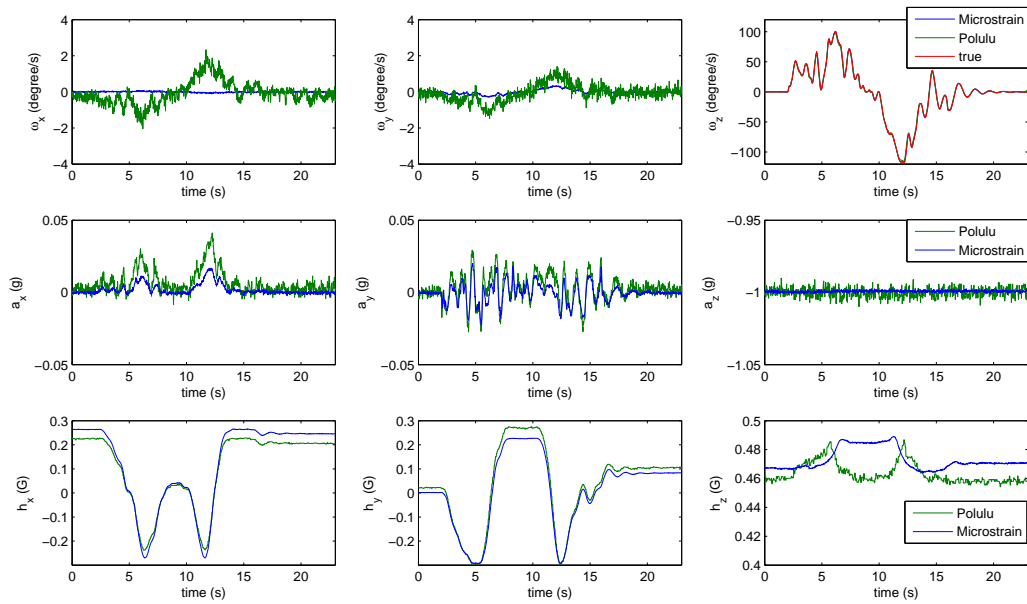


Figure 6.11: Measurements from IMUs and encoder.

Those measurements were saved and the attitude was estimated offline using these sensor inputs in the EKF loop. In order to compare the estimated attitude with the true one, the “true quaternions” were generated using equation (5.26). The encoder measurements were used as the yaw angle and zero degrees were assumed for the pitch and roll angles.

The next plots display the results obtained by the EKF estimation. In figure 6.12, it is presented a plot of the estimated quaternions using measurements of the MicroStrain sensor (in blue) and measurements of the Pololu sensor (in green). They are both compared with the “true quaternions”, obtained from the high precision encoder measurements. The second plot, shown in figure 6.13, is of the attitude angles roll (ϕ), pitch (θ) and yaw (ψ) obtained from the estimated quaternions. They are compared with the true measured angle of the encoder. Note that there is only measurements of the encoder in the yaw plot, since the rotation was performed about the z-axis.

A plot of the corresponding attitude covariances is shown in figure 6.14 while the covariances of the biases of the measurements are shown in figure 6.15 for the MicroStrain and in figure 6.16 for the Pololu. As expected, the covariances of the MicroStrain sensor are smaller than the Pololu’s.

Finally, the last plot presents the comparison of the angle of rotation errors ($\delta\theta_r$), see equation (6.3). The firsts 4 seconds were eliminated in order to wait for the filter to converge before analyzing the errors. Besides the green and blue plots showing the errors of the attitude estimation using real measurements from MicroStrain’s and Pololu’s IMUs, there are also errors from the simulated sensors in black and ma-

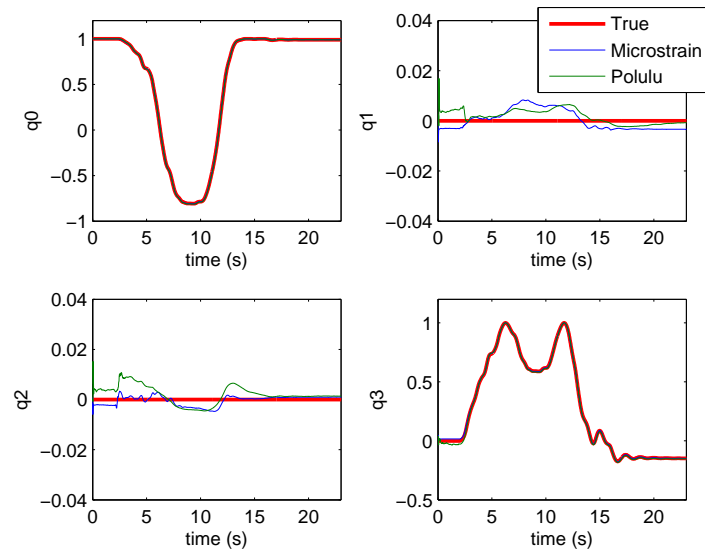


Figure 6.12: True and estimated quaternions.

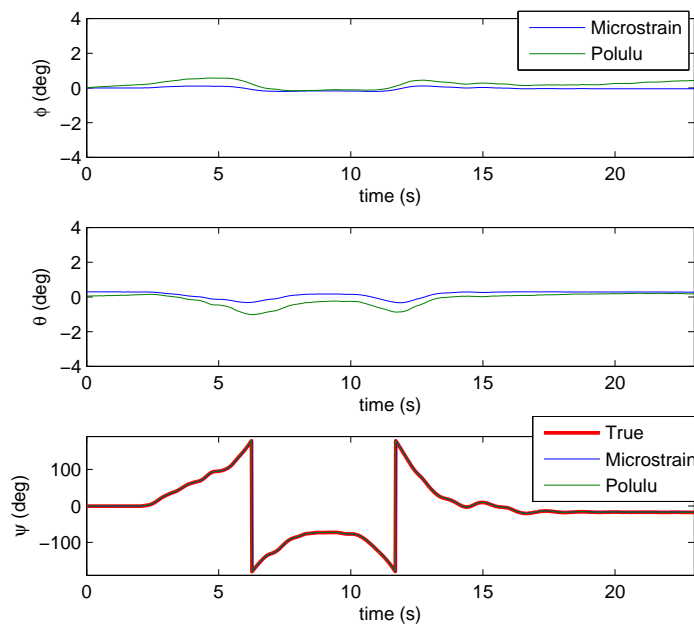


Figure 6.13: True and estimated Euler angles.

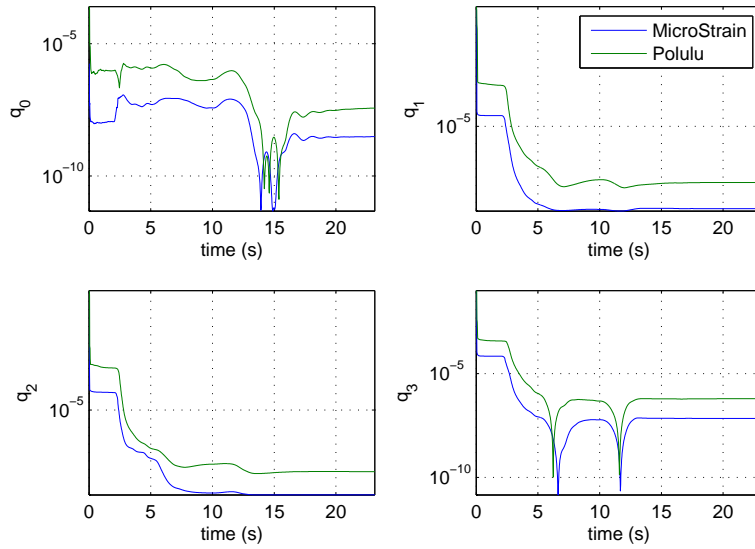


Figure 6.14: Covariances of the quaternions.

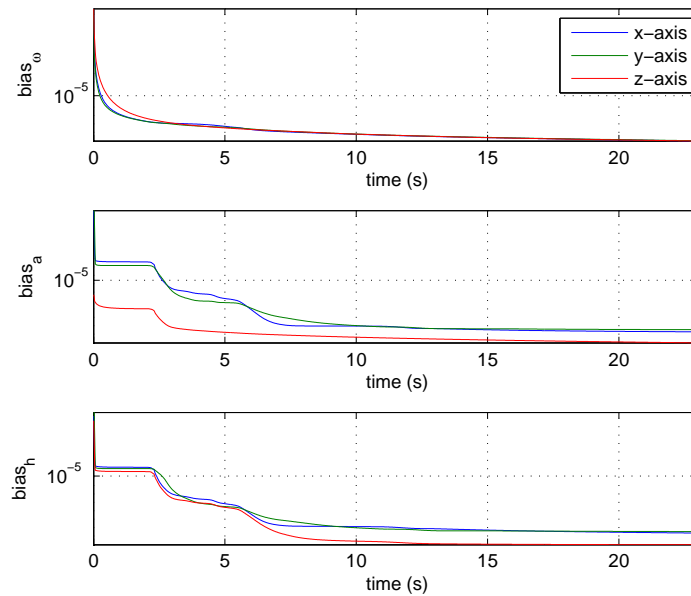


Figure 6.15: Covariances of the bias of the MicroStrain instrument.

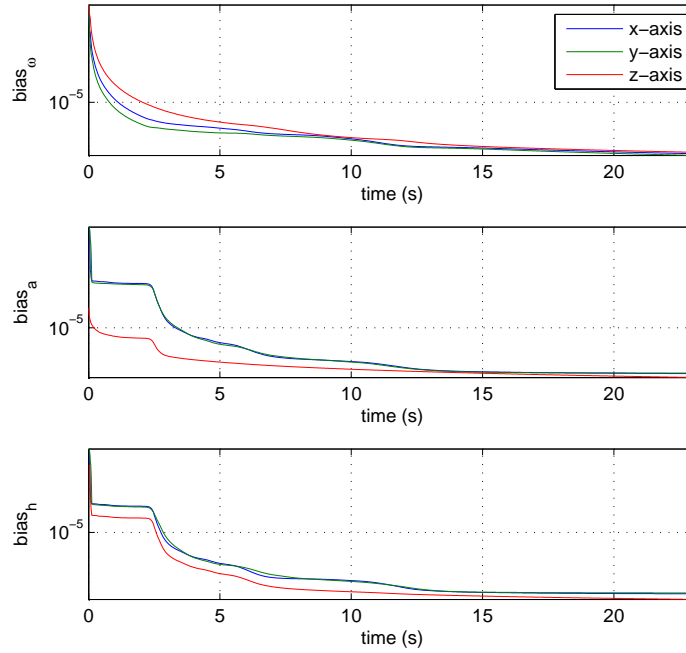


Figure 6.16: Covariances of the bias of the Pololu instrument.

genta.

All the sensors measurements were created in a simulation environment, as it was done in last section, with the difference that this time the “true quaternions” were derived from the encoder measurements, showed in red in figure (6.12). The simulated measurements served as an input to the EKF and the attitude was estimated and compared with the true one. The angle of rotation errors are shown in black for the Pololu’s noise variances and in magenta for the MicroStrain’s noise variances.

The mean values of the errors are:

- $\delta\bar{\theta}_r = 1.305^\circ$ for the MicroStrain real measurements.
- $\delta\bar{\theta}_r = 1.841^\circ$ for the Pololu real measurements.
- $\delta\bar{\theta}_r = 0.143^\circ$ for the MicroStrain simulated measurements.
- $\delta\bar{\theta}_r = 0.269^\circ$ for the Pololu simulated measurements.

The errors in the reality are much bigger than the simulated ones. It can be explained that the sensors were not perfectly level as expected. Observing figure 6.11, variations can be verified in the accelerations and angular velocities in the x-axis and y-axis, showing that there were movements in these directions.

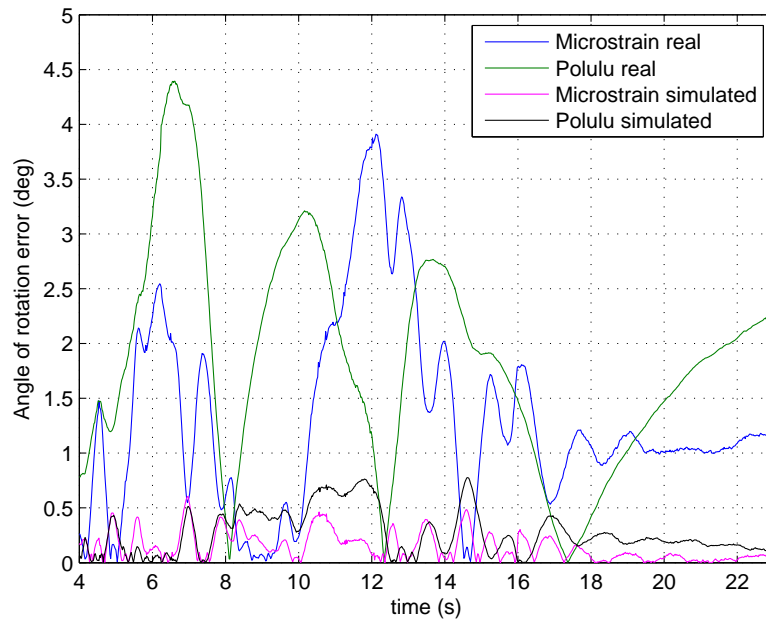


Figure 6.17: Angle of rotation errors of the test.

Also, variations in the magnetic field in the z-axis confirm this deduction. Hence, there were components of the movement not considered in the “true quaternion” simulation. For that reason, the errors were bigger: the estimation was just compared to “true values” that did not consider small rotations about the other axes.

Chapter 7

Conclusions and Future Work

7.1 Summary

This thesis presented a complete design of a sensor fusion solution using an extended Kalman filter for attitude determination.

A calibration procedure was developed and calibration parameters were obtained for two different IMUs. A sensor noise model was defined and obtained using the Allan variance method, which closely matched real data from angular rate, acceleration and magnetic field sensors.

Two approaches to the Kalman filter design were investigated. The first approach used quaternions and the second used modified Rodrigues parameters. Both approaches have similar computation demands to be implemented in a real time application and they produced similar results in a simulation environment. However, due to the singularity in 360 degrees of the MRP approach, the quaternion approach was chosen to be implemented in the satellite simulator since it has no singularities.

7.2 Analysis of Results

Both filters achieved results with a very good accuracy level in a simulation environment. Since the MicroStrain sensor simulations produced a better result in the attitude estimation, one conclusion that can be drawn is the lower is the noise characteristics of the sensor, more accurate is the attitude estimation.

Nevertheless, on the air bearing tests, the errors were higher than expected. There were several sources of errors which contributed to the high values obtained, including:

- The air bearing table was manually rotated, introducing oscillation caused by human interaction.

Additionally, the cables did not permitted the table to move freely. Moving the cables while rotating the sensors also may have contributed to introduce some vibrations in the measurements.

- The Pololu IMU was not rigidly fixed in the BB (see figure 6.10), making it susceptible to vibration. Also, the MicroStrain IMU was attached using just one screw, which could have caused the sensor to also move slightly during the rotation.
- The instruments used to level the platform were not accurate enough to make it completely flat with respect to the Earth.
- There are errors inherent to the sensors, not considered in the simple model formulated with white noise and bias drift.
- There are serious concern about the reliability of the magnetic information. The deviation of the sensed magnetic field magnitude from the local Earth's magnetic field magnitude can be very large depending on the amount of electromagnetic interference (in this case, the interferences are caused by cell phones, computers, power supplies, etc.). Therefore, the magnetometer is often used in conjunction with other sensors, as sun sensors or star cameras in order to correct for magnetic deviations.

Solutions for improving the accuracy of the filter using the real sensor are presented in the next section.

7.3 Future Work

The physical structure of satellite simulator is in assembly phase. Instead of the aluminum cube, the sensors will be mounted on the satellite structure in alignment with the body coordinate system of the satellite simulator. The deterministic sensor errors (misalignment, hard and soft iron effects, among others) must be corrected with new calibration parameters. Therefore, the calibration procedure described in Chapter 3 must be conducted again.

Some modifications can be done in the test procedure using the air bearing and IMUs to further improve the results. A few possibilities are as follows:

- Use high precision instruments to assure the air bearing is perfectly level.
- Rigidly attach the sensors to the satellite simulator structure.
- Perform the rotation using a motor to avoid the vibrations introduced by human hand.

- Eliminate the external cables, allowing the air bearing to rotate freely. In order to do so, power sources must be included in the satellite structure and the measurement data must be stored in the BB to be downloaded after the test is finished.

In addition to the inertial sensors, the satellite simulator is predicted to have a sun sensor and a star camera, which shall be included in the sensor fusion algorithm. These extra sensor are included with the goal to overcome the magnetometer inaccuracies and make the Kalman filter even more precise.

Finally, the Kalman filter will be implemented in a real-time environment and it will be used to estimate the position of the satellite in real-time. The attitude estimation is going to be used as an input by the control algorithm to keep the satellite in a desired orientation in the 3D space.

Bibliography

- [1] Bonnet, S., Bassompierre, C., Godin, C., Leseq, S., & Barraud, A. (2009). Calibration methods for inertial and magnetic sensors. *Sensors and Actuators A: Physical*, 156(2), 302–311.
- [2] Brown, R. G. (1983). *Introduction to Random Signal*. John Willey and Sons, New York.
- [3] Choukroun, D., Bar-Itzhack, I. Y., & Oshman, Y. (2006). Novel quaternion Kalman filter. *IEEE Transactions on Aerospace and Electronic Systems*, 42(1), 174–190.
- [4] Crassidis, J. L. & Junkins, J. L. (2004). *Optimal Estimation of Dynamics Systems*. Chapman & Hall/Crc, Boca Raton, Florida, First edition.
- [5] Crassidis, J. L., & Markley, F. L. (1996). Attitude Estimation Using Modified Rodrigues Parameters. *Proceedings of the Flight Mechanics/Estimation Theory Symposium, NASA-Goddard Space Flight Center* (pp. 71–83). Greenbelt.
- [6] Crassidis, J. L., Markley, F. L., & Cheng, Y. (2007). Survey of Nonlinear Attitude Estimation Methods. *Journal of Guidance Control and Dynamics*, 30(1), 12–28.
- [7] El-Sheimy, N., Hou, H., & Niu, X. (2008). Analysis and Modeling of Inertial Sensors Using Allan Variance. *IEEE Transactions on Instrumentation and Measurement*, 57(1), 140–149.
- [8] Flenniken, W. S. (2005). *Modeling Inertial Measurement Units and Analyzing the Effect of Their Errors in Navigation Applications*. Auburn University.
- [9] Flenniken, W. S., Wall, J. H., & Bevely, D. M. (2005). Characterization of various IMU error sources and the effect on navigation performance. *Proceedings of the Institute of Navigation GNSS conference*.
- [10] Hou, H. (2004). *Modeling inertial sensors errors using Allan variance*. University of Calgary.

- [11] Hung, J., Thacher, J., & White, H. (1989). Calibration of accelerometer triad of an IMU with drifting Z-accelerometer bias. In Proc. NAECON, IEEE Aerospace and Electronics Conference (Vol. 1, pp. 153–158).
- [12] Jerath, K., & Brennan, S. N. (2011). GPS-Free Terrain-Based Vehicle Tracking Performance as a Function of Inertial Sensor Characteristics. ASME 2011 Dynamic Systems and Control Conference and Bath/ASME Symposium on Fluid Power and Motion Control, Volume 2, 367–374.
- [13] Kalman, R. E. (1960). A New Approach to Linear Filtering and Prediction Problems. Transaction of the ASME - Journal of Basic Engineering, 35-45.
- [14] Kok, M., Hol, J. D., & Schon, T. B. (2012). Calibration of a magnetometer in combination with inertial sensors. Information Fusion (FUSION) (pp. 787–793). Singapore.
- [15] Kuipers, J.B. (1999) Quaternions and Rotation Sequences, Princeton University Press, Princeton, New Jersey.
- [16] Lefferts, E. J., Markley, F. L., & Shuster, M. D. (1982). Kalman Filter for Spacecraft Attitude Estimation. Orlando: AIAA.
- [17] Marins, J. L., Yun, X. Y. X., Bachmann, E. R., McGhee, R. B., & Zyda, M. J. (2001). An extended Kalman filter for quaternion-based orientation estimation using MARG sensors. Proceedings 2001 IEEEERSJ International Conference on Intelligent Robots and Systems Expanding the Societal Role of Robotics in the the Next Millennium, 4(2), 2003–2011.
- [18] Peter, B. (2011). Development of an Automatic IMU Calibration System. Swiss Federal Institute of Technology.
- [19] Renaudin, V., Afzal, M. H., & Lachapelle, G. (2010). Complete Triaxis Magnetometer Calibration in the Magnetic Domain. Journal of Sensors, 2010, 1–10.
- [20] Sabatini, A. M. (2006). Quaternion-based extended Kalman filter for determining orientation by inertial and magnetic sensing. IEEE Transactions on Biomedical Engineering, 53(7), 1346–1356.
- [21] Shuster, M. D. (1993). A Survey of Attitude Representations. The Journal of the Astronautical Sciences, 1(4), 439–517.
- [22] Simon, D. (2006). Optimal State Estimation. Hoboken, NJ, USA: John Wiley & Sons, Inc.

- [23] Skog, I., & Peter, H. (2006). Calibration of a MEMs inertial measurement unit. In XVII IMEKO World Congress on Metrology for a Sustainable Development. Rio de Janeiro.
- [24] Vasconcelos, J. F., Elkaim, G., & Silvestre, C. (2008). A geometric approach to strapdown magnetometer calibration in sensor frame. *Navigation, Guidance and Control of Underwater Vehicles*, 2(1), 1–11.
- [25] Wang, L., Hao, Y., Wei, Z., & Wang, F. (2010). A Calibration Procedure and Testing of MEMS Inertial Sensors for an FPGA-based GPS / INS System. *IEEE International Conference on Mechatronics and Automation* (pp. 1431–1436). Xi'an.
- [26] Welch, G. & Bishop, G. (2001). *An introduction to the Kalman filter*. University of North Carolina at Chapel Hill.
- [27] Yang, Y. (2012). Spacecraft attitude determination and control: Quaternion based method. *Annual Reviews in Control*, 36(2), 198–219.
- [28] Yun, X. Y. X., Aparicio, C., Bachmann, E. R., & McGhee, R. B. (2006). Design, Implementation, and Experimental Results of a Quaternion-Based Kalman Filter for Human Body Motion Tracking. *IEEE Transactions on Robotics*, 22(6), 1216–1227.
- [29] Zhao, Y., Horemuz, M., & Sjöberg, L. (2011). Stochastic modeling and analysis of IMU sensor errors. *Archives of Photogrammetry, Cartography and Remote Sensing*, 22, 437–449.
- [30] IEEE Std 647-2006. *IEEE Standard Specification Format Guide and Test Procedure for Single-Axis Laser Gyros* IEEE Aerospace and Electronic Systems Society. (2006). New York.
- [31] TN-I0025 MicroStrain Technical Note. (2011). Using the 3DM-GX3®-25 Capture Gyro Bias Function. Rev. 1.

Appendix A

Kalman Filter Matrices

A.1 First Approach

The matrix $\Xi_{4 \times 3}$ is defined as:

$$\Xi_{4 \times 3} = \begin{bmatrix} -q_1 & -q_2 & -q_3 \\ q_0 & -q_3 & q_2 \\ q_3 & q_0 & -q_1 \\ -q_2 & q_1 & q_0 \end{bmatrix}.$$

It simplifies the matrix representations of the other matrices. They are given by

$$F_k = \begin{bmatrix} F_{1_{4 \times 4}} & \vdots & -\frac{\Delta t_s}{2|q_k|} \Xi_{4 \times 3} & \vdots & 0_{4 \times 6} \\ \dots & \vdots & \dots & \dots & \dots \\ 0_{9 \times 4} & \vdots & & I_{9 \times 9} & \end{bmatrix},$$
$$W_k = \begin{bmatrix} -\frac{\Delta t_s}{2|q_k|} \Xi_{4 \times 3} & \vdots & 0_{4 \times 9} \\ \dots & \vdots & \dots \\ 0_{9 \times 3} & \vdots & \Delta t_s I_{9 \times 9} \end{bmatrix},$$

$$H_k = \begin{bmatrix} 2a_y^l q_3 - 2a_z^l q_2 & 2a_y^l q_2 + 2a_z^l q_3 & 2a_y^l q_1 - 4a_x^l q_2 - 2a_z^l q_0 & 2a_y^l q_0 - 4a_x^l q_3 + 2a_z^l q_1 & \vdots & \vdots \\ 2a_z^l q_1 - 2a_x^l q_3 & 2a_x^l q_2 - 4a_y^l q_1 + 2a_z^l q_0 & 2a_x^l q_1 + 2a_z^l q_3 & 2a_z^l q_2 - 4a_y^l q_3 - 2a_x^l q_0 & \vdots & \vdots \\ 2a_x^l q_2 - 2a_y^l q_1 & 2a_x^l q_3 - 2a_y^l q_0 - 4a_z^l q_1 & 2a_x^l q_0 + 2a_y^l q_3 - a_z^l q_2 & 2a_x^l q_1 + 2a_y^l q_2 & \vdots & 0_{6 \times 3} \\ 2h_y^l q_3 - 2h_z^l q_2 & 2h_y^l q_2 + 2h_z^l q_3 & 2h_y^l q_1 - 4h_x^l q_2 - 2h_z^l q_0 & 2h_y^l q_0 - 4h_x^l q_3 + 2h_z^l q_1 & \vdots & \vdots \\ 2h_z^l q_1 - 2h_x^l q_3 & 2h_x^l q_2 - 4h_y^l q_1 + 2h_z^l q_0 & 2h_x^l q_1 + 2h_z^l q_3 & 2h_z^l q_2 - 4h_y^l q_3 - 2h_x^l q_0 & \vdots & \vdots \\ 2h_x^l q_2 - 2h_y^l q_1 & 2h_x^l q_3 - 2h_y^l q_0 - 4h_z^l q_1 & 2h_x^l q_0 + 2h_y^l q_3 - a_z^l q_2 & 2h_x^l q_1 + 2h_y^l q_2 & \vdots & \vdots \end{bmatrix}.$$

The term $F1_{4 \times 4}$ is simply the partial derivatives of the equation (5.12) with respect to the quaternions. The result is quite complicated, therefore just the element 1,1 of the matrix is written here.

$$F1_{1,1} = \frac{1}{|q_k|} - \frac{q_0}{|q_k|^3} (q_0 - \frac{\Delta t_s}{2} (q_1(\tilde{\omega}_{x,k} - \beta_{x,\omega k}) + q_2(\tilde{\omega}_{y,k} - \beta_{y,\omega k}) + q_3(\tilde{\omega}_{z,k} - \beta_{z,\omega k}))) \frac{1}{|q_k|^3}.$$

A.2 Second Approach

The matrix $\Gamma_{3 \times 3}$ is defined as:

$$\Gamma_{3 \times 3} = \begin{bmatrix} 0 & p_3 - p_1 p_2 & -p_2 - p_1 p_3 \\ -p_3 - p_1 p_2 & 0 & p_1 - p_2 p_3 \\ p_2 - p_1 p_3 & -p_1 - p_2 p_3 & 0 \end{bmatrix}.$$

It is used to compose the Kalman filter matrices as shown below:

$$F_k = \begin{bmatrix} F1_{3 \times 3} & \vdots & \frac{\Delta t_s}{2} (\frac{p_1^2}{2} - \frac{p_2^2}{2} + \frac{p_3^2}{2} - \frac{1}{2}) I_{3 \times 3} + \Gamma_{3 \times 3} & \vdots & 0_{3 \times 6} \\ \dots & \vdots & \dots & \dots & \dots \\ 0_{9 \times 3} & \vdots & I_{9 \times 9} & \vdots & \dots \end{bmatrix},$$

$$W_k = \begin{bmatrix} \frac{\Delta t_s}{2} (\frac{p_1^2}{2} - \frac{p_2^2}{2} + \frac{p_3^2}{2} - \frac{1}{2}) I_{3 \times 3} + \Gamma_{3 \times 3} & \vdots & 0_{3 \times 9} \\ \dots & \vdots & \dots \\ 0_{9 \times 3} & \vdots & \Delta t_s I_{9 \times 9} \end{bmatrix},$$

$$H_k = \begin{bmatrix} H1_{6 \times 3} & \vdots & 0_{6 \times 3} & \vdots & I_{6 \times 6} \end{bmatrix}.$$

The term $F1_{4 \times 4}$ is simply the partial derivatives of the equation (5.4) with respect to the MRP. The

result is quite complicated, therefore just the element 1,1 of the matrix is written here.

$$F1_{1,1} = 1 + \frac{\Delta t_s}{2} (p_1(\tilde{\omega}_{x,k} - \beta_{x,\omega k}) + p_2(\tilde{\omega}_{y,k} - \beta_{y,\omega k}) + p_3(\tilde{\omega}_{z,k} - \beta_{z,\omega k})).$$

Also complicated is the term $H1_{6 \times 3}$, the result of the partial derivatives of equation (5.18) with respect to the MRP.

$$H1_{1,1} = \frac{8(a_y(p_2 - p_1 p_3) + a_z(p_3 + p_1 p_2))}{(p_1^2 + p_2^2 + p_3^2 + 1)^2} + \frac{-32(p_1^2 p_2 a_y + p_1^2 p_3 a_z - a_x p_1 (p_2^2 + p_3^2)) + 16(p_1 p_3 a_y - p_1 p_2 a_z)(p_1^2 + p_2^2 + p_3^2 - 1)}{(p_1^2 + p_2^2 + p_3^2 + 1)^3}.$$